



## Article

# Petrogenesis of the Shibaogou Mo-W-Associated Porphyritic Granite, West Henan, China: Constrains from Geochemistry, Zircon U-Pb Chronology, and Sr-Nd-Pb Isotopes

Zhiwei Qiu <sup>1</sup>, Zhenju Zhou <sup>2,3,\*</sup>, Nan Qi <sup>4</sup>, Pocheng Huang <sup>1</sup>, Junming Yao <sup>5</sup> , Yantao Feng <sup>6</sup> and Yanjing Chen <sup>1,5,\*</sup> 

<sup>1</sup> Key Laboratory of Crustal and Orogenic Evolution, Peking University, Beijing 100871, China; zwqiu@pku.edu.cn (Z.Q.)

<sup>2</sup> Institute of Geomechanics, Chinese Academy of Geological Sciences, Beijing 100081, China

<sup>3</sup> Key Laboratory of Paleomagnetism and Tectonic Reconstruction of Ministry of Natural Resources, Beijing 100081, China

<sup>4</sup> State Key Laboratory of Continental Dynamics, Department of Geology, Northwest University, Xi'an 710069, China

<sup>5</sup> Xinjiang Research Center for Mineral Resources, Xinjiang Institute of Ecology and Geography, Chinese Academy of Sciences, Ürümqi 830011, China

<sup>6</sup> Henan Xiangyan Mining Ltd., Zhengzhou 450016, China

\* Correspondence: zhenjuzhou@126.com (Z.Z.); yjchen@pku.edu.cn (Y.C.)

**Abstract:** The Shibaogou pluton, located in the Luanchuan orefield of western Henan Province in China, is a typical porphyritic granite within the Yanshanian “Dabie-type” Mo metallogenic system. It is mainly composed of porphyritic monzogranite and porphyritic syenogranite. Zircon U-Pb dating results indicate emplacement ages of  $150.1 \pm 1.3$  Ma and  $151.0 \pm 1.1$  Ma for the monzogranite and  $148.1 \pm 1.0$  Ma and  $148.5 \pm 1.3$  Ma for the syenogranite. The pluton is characterized by geochemical features of high silicon, metaluminous, and high-K calc-alkaline compositions, enriched in Rb, U, Th, and Pb, and exhibits high Sr/Y (18.53–58.82), high (La/Yb)<sub>N</sub> (9.01–35.51), and weak Eu anomalies. These features indicate a source region from a thickened lower crust with garnet and rutile as residual phases at depths of approximately 40–60 km. Sr-Nd-Pb isotopic analyses suggest that the magmatic source is mainly derived from the Taihua and Xiong'er Groups of the Huaxiong Block, mixed with juvenile crustal rocks from the Kuanping and Erlangping Groups of the North Qinling Accretion Belt. Combined with geological and isotopic characteristics, it is concluded that the Shibaogou pluton formed during the compression–extension transition period associated with the collision between the Yangtze Block and the North China Craton, reflecting the complex partial melting processes in the thickened lower crust. The present study reveals that the magmatic–hydrothermal activity at Shibaogou lasted approximately 5 Ma, showing multi-phase characteristics, further demonstrating the close relationship between the pluton and the Mo-W mineralization.

**Keywords:** Shibaogou pluton; Qinling Orogen; trace elements; zircon U-Pb dating; Sr-Nd-Pb isotopes



**Citation:** Qiu, Z.; Zhou, Z.; Qi, N.; Huang, P.; Yao, J.; Feng, Y.; Chen, Y. Petrogenesis of the Shibaogou Mo-W-Associated Porphyritic Granite, West Henan, China: Constrains from Geochemistry, Zircon U-Pb Chronology, and Sr-Nd-Pb Isotopes. *Minerals* **2024**, *14*, 1173. <https://doi.org/10.3390/min14111173>

Academic Editor: Giorgio Garuti

Received: 17 October 2024

Revised: 10 November 2024

Accepted: 17 November 2024

Published: 19 November 2024



**Copyright:** © 2024 by the authors. Licensee MDPI, Basel, Switzerland. This article is an open access article distributed under the terms and conditions of the Creative Commons Attribution (CC BY) license (<https://creativecommons.org/licenses/by/4.0/>).

## 1. Introduction

Porphyry molybdenum deposits are the primary source of global molybdenum resources. The study of the metallogenic models of these deposits has long been a focus, particularly concerning the characteristics of ore-forming intrusions. Traditionally, two major metallogenic models, the Climax-type (back-arc rift-related type) and Endako-type (continental arc-related type), have dominated research on molybdenum deposits in accretionary orogenic belts. Climax-type molybdenum deposits generally exhibit high Mo grades and form in the early stage of back-arc extension induced by oceanic crust subduction. The process is accompanied by fluorine-rich, highly differentiated rhyolitic-alkaline magmatism [1,2]. In contrast, Endako-type molybdenum deposits are more common, characterized by low-grade Mo deposits that form in continental margin arc settings. These

deposits result from partial melting of oceanic crust and mantle wedge, associated with fluorine-poor calc-alkaline magmatism [3,4].

In contrast, a large number of molybdenum deposits in China are distributed within intracontinental collisional orogenic belts, where the metallogenic characteristics differ significantly from those formed in oceanic-continental subduction settings. The ore-forming fluids of these deposits typically exhibit high F/Cl, K/Na, and CO<sub>2</sub>/H<sub>2</sub>O ratios with the development of multi-phase CO<sub>2</sub>-rich fluid inclusions, and the magma source is attributed to the remelting of ancient crust [5–7]. This distinctive metallogenic model is known as the “Collision-type” or “Dabie-type” porphyry molybdenum deposit [6,8]. The model addresses a gap in the understanding of metallogenesis in continental collision zones and provides a significant complement to the traditional Climax-type and Endako-type models.

Despite this, due to the limited geochemical data on ore-causative igneous rocks, the understanding of the metallogenic mechanisms and the genesis of intrusions in Dabie-type molybdenum deposits remains less developed compared to Climax-type and Endako-type deposits [9]. The Luanchuan orefield in the Eastern Qinling Orogen, known as the “Molybdenum Capital of China”, hosts four super-large and several large- to medium-sized molybdenum deposits, with total resources exceeding 4.7 million tons. These porphyry-skarn-type molybdenum deposits were formed around 145 Ma, and all belong to the Dabie-type Mo deposit system. However, various hypotheses have been proposed regarding the genesis and source of the ore-forming intrusions, including crust-mantle mixing [10,11], remelting of the lower crust of the Huaxiong Block [12–14], and remelting of the Yangtze Plate [15]. As for the tectonic setting of magmatism and mineralization, the main perspectives include the compression–extension transition during the collisional orogeny [6,13,14,16], post-orogenic extension [17], and subduction of the western Pacific Plate [10,11,18].

The Shibaogou intrusion is the largest exposed pluton in the Luanchuan orefield and serves as the ore-causative intrusion for the Shibaogou–Zhuyuangou–Dawanggou Mo–W deposits. Previous studies on its emplacement age have yielded two groups of results: 156–157 Ma [19] and 145–149 Ma [14,15,20]. Moreover, significant debate exists regarding its genesis, particularly in terms of whether the intrusion originated from the remelting of the Huaxiong Block or Yangtze Plate and whether mantle-derived mafic magma mixing was involved. To address these controversies, the present study provides new geochemical data for the Shibaogou intrusion, including zircon U–Pb ages, whole-rock major and trace elements, and Sr–Nd–Pb isotopes. The characteristics, source, and genesis of the intrusion are discussed based on these new data. These findings offer valuable evidence for further constraining the genesis and tectonic background of the Yanshanian ore-forming intrusions in the Luanchuan orefield.

## 2. Regional Geology

The Qinling Orogen forms the core of the Central China orogen and is the largest molybdenum metallogenic belt in the world (Figure 1a) [6]. Following the closure of the Paleo-Tethys Ocean around 200 Ma, a collision orogeny occurred between the Yangtze Plate and the North China Craton, eventually resulting in the formation of the Qinling Orogen [21–23]. The Qinling Orogen is bounded to the north by the Sanmenxia–Baofeng Fault and to the south by the Longmenshan–Dabashan Fault. From north to south, it is divided into four tectonic units: the Huaxiong Block, the North Qinling Accretion Belt, the South Qinling Fold Belt, and the Songpan Fold Belt, separated by the Luanchuan Fault, the Shangdan Fault, and the Mianlve Fault (suture zone), respectively (Figure 1b) [6]. The Luanchuan orefield is located in the southern part of the Huaxiong Block, northwest of Luanchuan County, and is separated from the North Qinling Accretion Belt by the Luanchuan Fault.

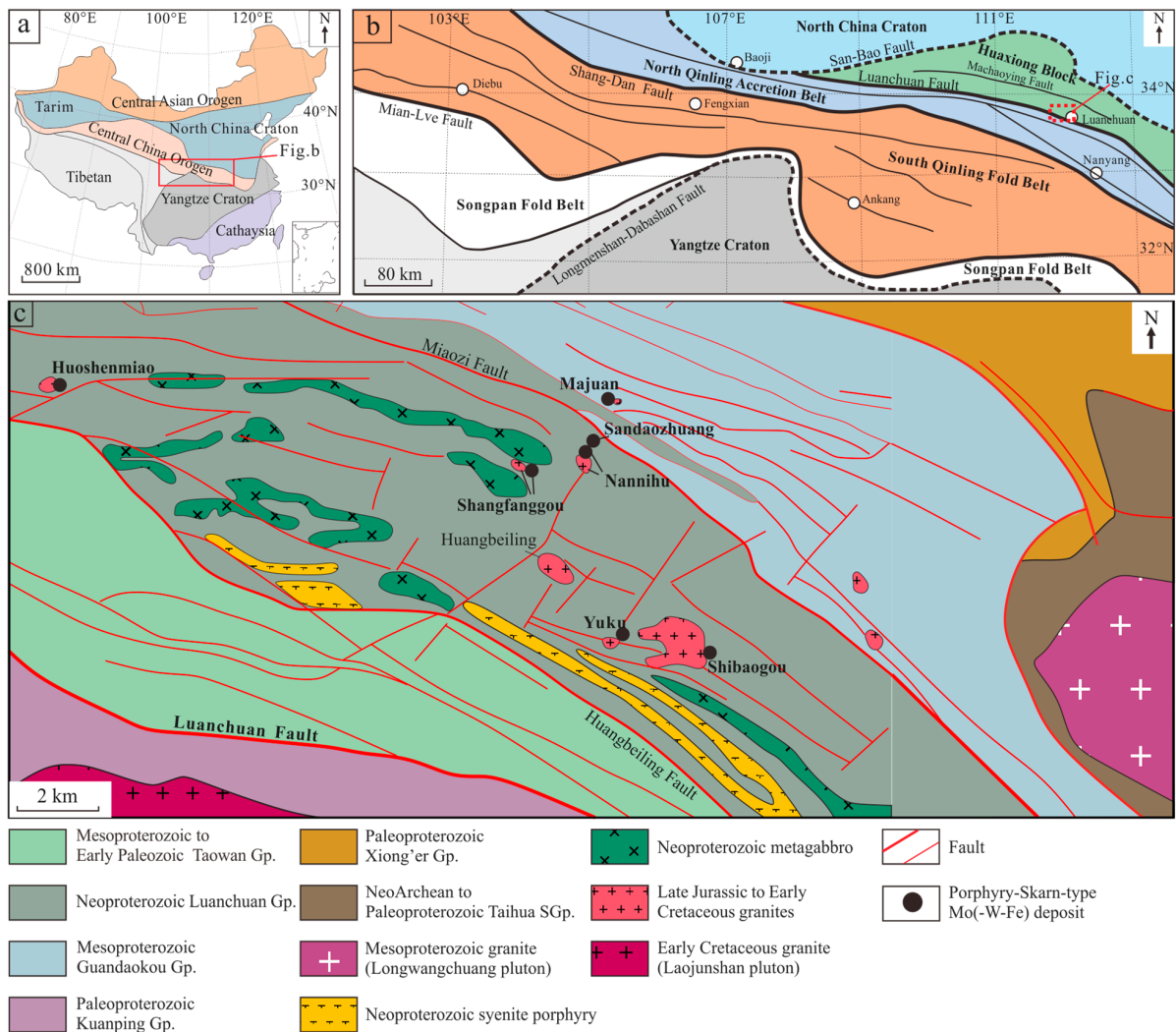


**Figure 1.** (a) Tectonic subdivision map of China, showing the location of the Qinling Orogen (modified after [24]); (b) tectonic subdivision map of the Qinling Orogen, showing the location of the Luanchuan orefield (modified after [24]); (c) geological map of Luanchuan orefield, showing the granitoid and deposits distribution (modified after [25]).

The Huaxiong Block exhibits a double-layered crustal structure. The basement, Neoproterozoic to Paleoproterozoic Taihua Supergroup, consists of TTG rocks, marbles, and migmatites metamorphosed under high amphibolite- to granulite-facies conditions [26]. The Taihua Supergroup formed between 3.0 and 2.1 Ga and underwent metamorphism during 1.95–1.85 Ga [26–28]. The cover sequences comprise the Paleoproterozoic Xiong'er Group, Mesoproterozoic Guandaokou Group, Neoproterozoic Luanchuan Group, and Mesoproterozoic to Early Paleozoic Taowan Group. The Xiong'er Group is mainly composed of andesite to rhyolite with a few sedimentary rocks, formed during 1.78–1.45 Ga (peak at 1.78–1.75 Ga) [29,30]. Both the Guandaokou and Luanchuan Groups are composed of clastic-carbonate sedimentary sequences [31]. The Guandaokou Group is mainly distributed in the northern part of the study area, characterized by dolomitic marbles and fine-grained clastic rocks. The Luanchuan Group is the main exposed strata in the study area (Figure 1c) and can be subdivided into four formations based on the sedimentary sequence (Figure 2): the Baishugou Formation (carbonaceous slate and quartz phyllite), the Sanchuan Formation (marble, sandstone), the Nannihu Formation (quartz sandstone and siliceous marble), and the Meiyaogou Formation (dolomitic marble and carbonaceous slate). The Taowan Group, dominated by limestone, phyllite, meta-sandstone, and quartzite

lithologies, is widely distributed along the southern boundary zone of the Luanchuan ore-field, commonly interpreted as an olistostrome zone marking the separation between the Huaxiong Block and North Qinling Accretion Belt, i.e., the Luanchuan Fault zone [6]. To the south of the Luanchuan Fault, the North Qinling Accretion Belt mainly consists of the Qinling Group high-grade metamorphic rocks as the basement and the Kuanping and Erlangping Groups as the cover. The Kuanping Group represents the Paleoproterozoic ophiolite, and the Erlangping Group comprises Neoproterozoic to Early Paleozoic metavolcanic and sedimentary rocks [32].

The NWW-trending structures, with the Luanchuan Fault as a representation, are the primary ore-controlling structures in the region (Figure 1c) [12,33]. During the Mesozoic continental collision, the Luanchuan Fault served as an intracontinental subduction zone, resulting in horizontal shortening and vertical thickening of the crust. Its subsidiary NNE-trending faults provided favorable structural space for mineralization.

The exposed igneous rocks in the studied area include Neoproterozoic gabbro, syenite porphyry, and Yanshanian granites (Figure 1c). The latter, such as Shibaogou, Yuku, Nannihu, and Shangfanggou, primarily intruded into the Luanchuan Group and were widely associated with Mo-W mineralization [33].

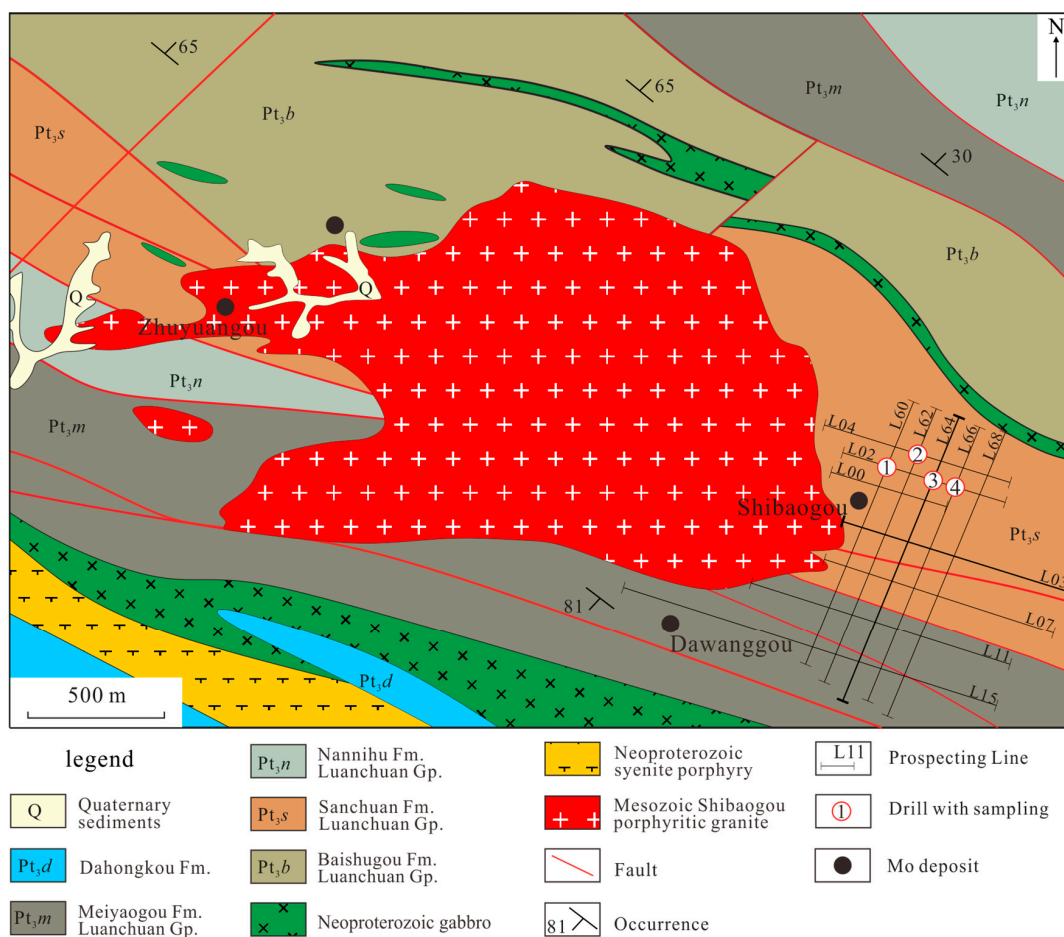


**Figure 2.** Geological map of Shibaogou deposit (modified after [34]). The number of drill holes: 1. ZK6002; 2. ZK6204; 3. ZK6402; 4. ZK6602.

### 3. Deposit and Pluton Geology

The Shibaogou molybdenum deposit is located ~8 km west of Luanchuan County, Henan Province, and is primarily distributed around the Shibaogou pluton (Figure 2). The main strata in the area consist of marble from the Sanchuan Formation, carbonaceous slate and siltstone from the Baishugou Formation of the Luanchuan Group. Due to the



large exposed area of the Shibaogou intrusion, several related deposits have formed, including the Shibaogou deposit on the east of the intrusion (with five ore bodies, more than  $20 \times 10^4$  tons of Mo) [34], the Shibaogou Mo-W ore block on the northwest of the intrusion (with three ore bodies) [35], the Zhuyuangou deposit in the west of the intrusion (with proven  $14.3 \times 10^4$  tons of Mo and  $17.1 \times 10^4$  tons of  $WO_3$ ) [36], and the Dawanggou deposit to the southeast of the intrusion [37]. The Shibaogou deposit has proven Mo reserves that meet the criteria for a large-scale deposit, with further potential for expansion as deep exploration is ongoing [35]. Samples for the present study were collected from drill cores in the Shibaogou deposit on the eastern side of the intrusion (Figure 2).

### 3.1. Feature of Orebody and Alteration

The ore bodies of the Shibaogou deposit are hosted within the outer contact zones between the intrusion and the wallrocks, as well as in relatively flat areas near the concealed top of the intrusion. The ore bodies display an irregular elliptical shape in plan view and appear layered in profile with local thickening. The overall dip is toward the NEE. The bottom boundary of the ore bodies roughly aligns with the top of the granite porphyry, with a dip angle generally around  $30^\circ$  (Figure 3) [34]. Preliminary estimates indicate that the Mo reserves more than  $20 \times 10^4$  tons, with an average grade of 0.05%–0.10%.

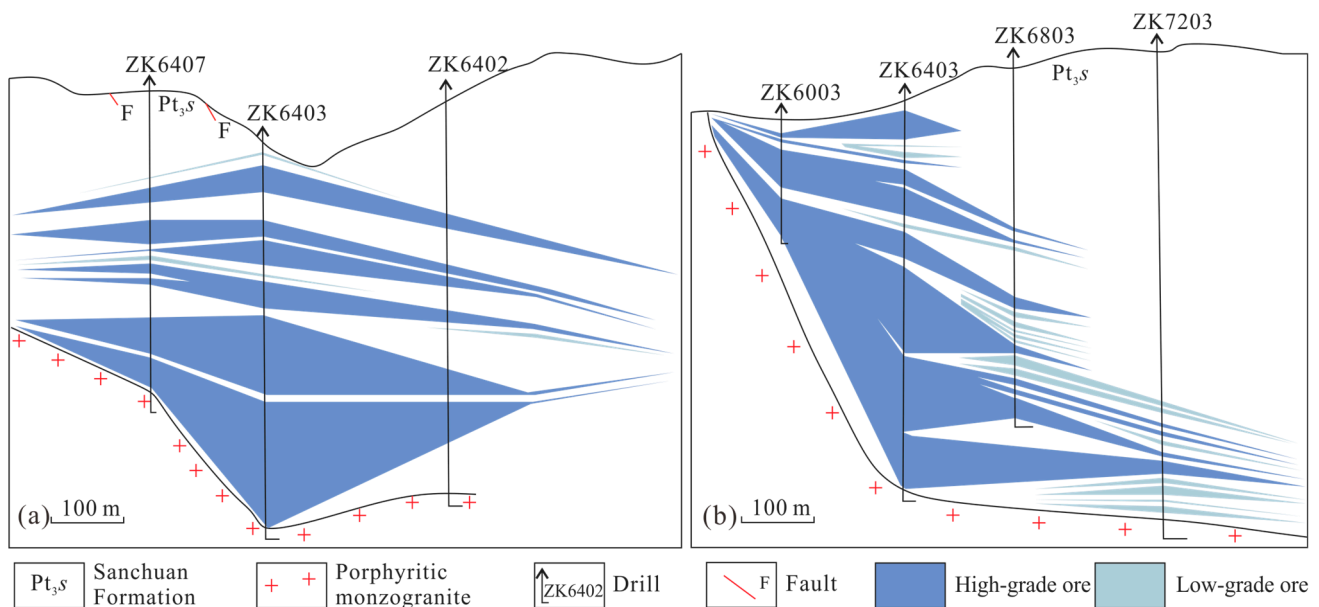


**Figure 3.** Geological profiles for prospecting lines L64 (a) and L03 (b) of the Shibaogou deposit [34].

The wallrock alteration is primarily concentrated along the contact zones. The alteration in the outer contact zone is more intense and broader than that in the inner contact zone. The main types of alteration include potassic alteration, hornfelsing, and skarn-type alteration, superimposed with silicification, sericitization, fluorite alteration, and late-stage carbonation. The main ore minerals are represented by molybdenite, scheelite, galena, and sphalerite, while the gangue minerals comprise quartz, garnet, chlorite, and fluorite. Molybdenite occurs in disseminated, vein-like, or massive structures, while scheelite typically occurs in disseminated structures, coexisting with garnet and other skarn minerals.

### 3.2. Petrography of Shibaogou Pluton

The main lithology of the Shibaogou intrusion is monzogranite, followed by syenogranite, both of which are closely related to mineralization and commonly exhibit K-feldspar alteration. The deeper parts of the intrusion contain granodiorite, which shows weaker alteration and has no obvious connection to mineralization. Below is a description of the petrography of the monzogranite and syenogranite.

The porphyritic monzogranite displays a massive structure (Figure 4a). The phenocrysts mainly consist of K-feldspar, quartz, and plagioclase, while the matrix exhibits medium- to fine-grain with a granitic texture (Figure 4b,c). The K-feldspar (contents ~35%) is predominantly orthoclase with a small amount of microcline, with grain sizes of 1–2 cm for phenocryst and 0.2–0.8 cm for that in the matrix. Carlsbad twinning is commonly observed. Plagioclase (20%–25%) is mainly andesine and oligoclase, subhedral and tabular, with a grain size of 0.2–1 cm. Quartz has a grain size of ~1 cm for phenocrysts, while that in the matrix range from 0.2 to 0.5 cm, with a content of 30%–35%. Biotite is euhedral, with grain sizes of 0.3–0.7 cm and a content of about 5% (Figure 4b). Among the accessory minerals (<1%), apatite is common, with occasional zircon and titanite observed. Epidotization and chloritization are developed in the contact zone between the intrusion and wallrocks. Sample 6602-7 shows strong hydrolysis alteration, manifested as sericitization to kaolinization of K-feldspar and plagioclase, with moderate to strong chloritization of biotite along cleavage planes (Figure 4d). Some samples (6204-49 and 6002-2) exhibit strong K-feldspar alteration, characterized by the formation of numerous fine orthoclase crystals in the matrix. Some plagioclase phenocrysts have transformed into orthoclase, while orthoclase phenocrysts remain not affected by alteration (Figure 4e,f).

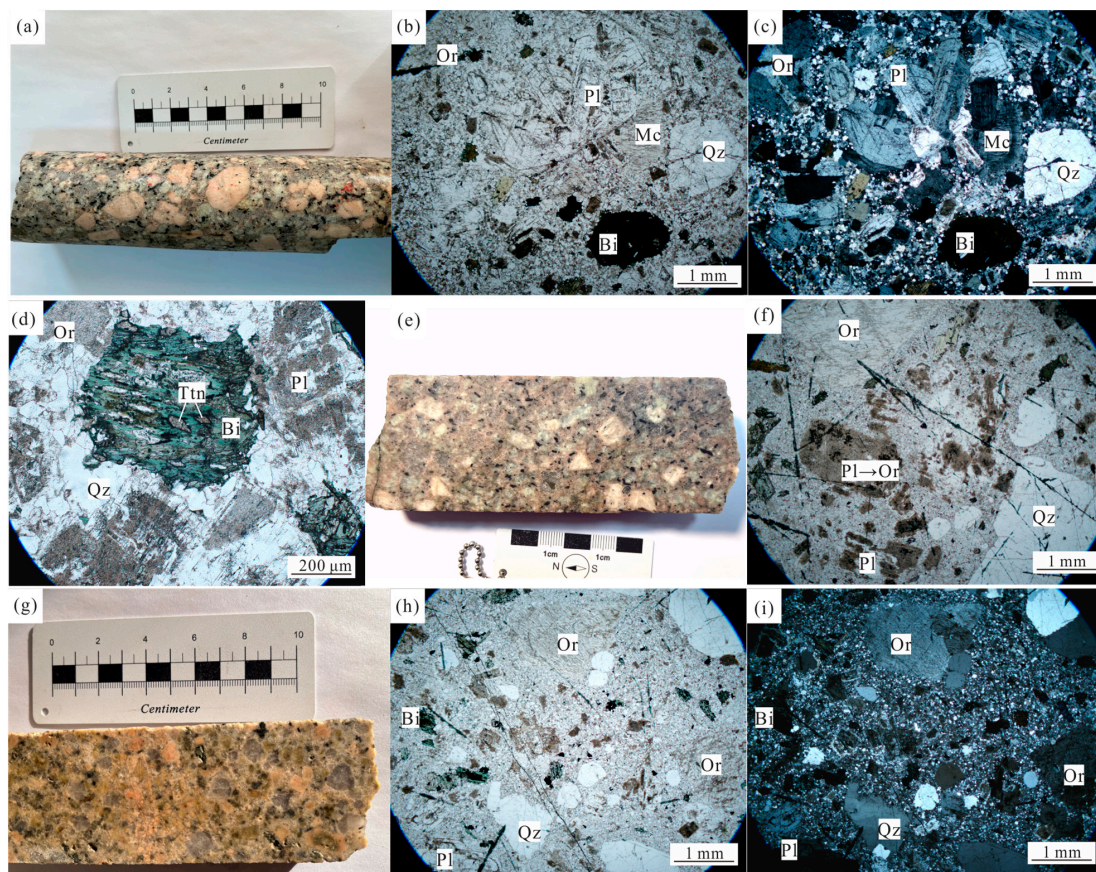


**Figure 4.** Photographs showing petrography of the Shibaogou granite. (a) Hand specimen of monzogranite; (b) monzogranite under plane-polarized light (PPL), with euhedral-tabular plagioclase phenocrysts and anhedral microcline and quartz; (c) monzogranite under crossed-nicols light (CN); (d) sericitized monzogranite (PPL), with chloritized biotite and sericitized–kaolinized orthoclase; (e) hand specimen of K-feldspar-altered monzogranite; (f) K-feldspar alteration in monzogranite (PPL), with plagioclase phenocrysts altered to orthoclase, while orthoclase phenocrysts remain unaltered; (g) hand specimen of syenogranite; (h) microphotograph of syenogranite (PPL), with anhedral quartz and orthoclase phenocrysts as the main components; (i) microphotograph of syenogranite (CN). Mineral abbreviations: Bi. biotite; Mc. microcline; Or. orthoclase; Pl. plagioclase; Qz. quartz; Ttn. titanite.

The porphyritic syenogranite displays a massive structure (Figure 4g). The phenocrysts are mainly composed of K-feldspar and quartz, with fewer plagioclase. The matrix exhibits a fine-grained granitic texture (Figure 4h,i). The K-feldspar (contents ~40%) is predominantly orthoclase with a small amount of microcline, with grain sizes of 1–1.5 cm for phenocryst and 0.2–0.6 cm for that in the matrix. Plagioclase (~15%) is subhedral and tabular, with a grain size of 0.2–1 cm. Carlsbad–albite twinning, zoning structures, and sericitization are commonly observed. Quartz is anhedral and constitutes approximately 35%–40% of the rock. Biotite, with a grain size of 0.2–0.8 cm, accounts for about 2% and exhibits chloritization and pyritization. Accessory minerals are mainly apatite, with occasional zircon, titanite, and calcite. Epidotization is developed in the contact zone between the granite and the wallrocks.

#### 4. Samples and Analytical Methods

Six porphyritic monzogranite samples and five porphyritic syenogranite samples were collected from drill cores in the Shibaogou deposit. The porphyritic monzogranite samples were taken from drill hole ZK6602 at depths of 720 m and 490 m (sample numbers 6602-11 and 6602-7), drill hole ZK6204 at depths of 360 m, 410 m, and 530 m (sample numbers 6204-25, 6204-49, and 6204-60), and drill hole ZK6002 at a depth of 450 m (sample number 6002-2). The porphyritic syenogranite samples were collected from drill hole ZK6402 at depths of 520 m, 560 m, and 600 m (sample numbers 6402-34, 6402-35, and 6402-36), drill hole ZK6002 at a depth of 380 m (sample number 6002-1), and drill hole ZK6204 at a depth of 490 m (sample number 6204-58). Major and trace elements, as well as Sr-Nd-Pb isotope analyses, were conducted on these samples, along with zircon U-Pb dating. The analytical work was carried out by Beijing GeoAnalysis Co., Ltd., Beijing, China, while data processing was performed by the authors.

Zircon separation and target preparation were conducted for four samples: 6602-11, 6204-60, 6402-36, and 6002-1. Microscopic photography under transmitted light, reflected light, and cathodoluminescence (CL) was performed. Zircon U-Pb dating was accomplished using laser ablation–inductively coupled plasma mass spectrometry (LA-ICPMS), employing a NWR193UC model laser ablation system (Elemental Scientific Lasers LLC, Bozeman, MT, USA) coupled to an Agilent 7900 ICPMS (Agilent, Santa Clara, CA, USA). Detailed tuning parameters followed Thompson [38]. The analysis was performed using a 30 µm diameter spot at 6 Hz and a fluence of 5 J/cm<sup>2</sup>. Data processing was conducted using the Iolite software. Generally, 45 s of the sample signals were acquired after 25 s blank background measurement, and downhole fractionation was corrected using an exponential equation [39]. Isoplot software 3.70 [40] was used for age calculation and Concordia diagram drawing.

Elemental and isotopic analyses were conducted on 11 samples. Prior to analysis, the samples were washed and ground to below 200 mesh. Major elements and trace elements were tested using X-ray fluorescence (XRF-1800, SHIMADZU) and ICP-MS (Agilent 7500), respectively. The testing accuracy was better than 5% for major elements and better than 10% for trace elements. Detailed procedures can be referenced in Guo [12].

Whole-rock Sr and Nd isotopic analyses were performed using a Nu Plasma II MC-ICP-MS. Prior to analysis, chemical separation was conducted using anion exchange column methods, following the procedures described by Yang [41]. The <sup>87</sup>Sr/<sup>86</sup>Sr ratios were normalized to <sup>88</sup>Sr/<sup>86</sup>Sr = 8.37521 using exponential correction. Repeated precision monitoring tests were performed on the Sr isotope international standard NBS 987 to correct for instrumental drift. The <sup>143</sup>Nd/<sup>144</sup>Nd ratios were normalized to <sup>146</sup>Nd/<sup>144</sup>Nd = 0.7219, with GSB Nd as the internal standard. International basalt standards BCR-2 and Jndi-1 were used as unknown samples for quality control. The measured <sup>87</sup>Sr/<sup>86</sup>Sr ratio is 0.710244 ± 0.000012 (2σ) for NBS 987, and 0.704993 ± 0.000014 (2σ) for basalt BCR-2. For the Nd isotope standards, the measured <sup>143</sup>Nd/<sup>144</sup>Nd ratio was 0.512445 ± 0.000008 (2σ) for GSB, and 0.512112 ± 0.000008 (2σ) for Jndi-1, all within the recommended error ranges.



Lead isotopes in the samples were separated using BioRad AG MP-1 anion exchange columns, and the elemental concentrations were measured using an Agilent 7900 ICP-MS. A diluted solution (50 ppb Pb doping with 10 ppb Tl) was introduced into Neptune XT MC-ICP-MS (Bremen, Germany) through the Cetac Aridus III desolvating nebulizer system. The mass fractionation was corrected using  $^{205}\text{Tl}/^{203}\text{Tl} = 2.3885$ , with the international Pb isotope standard NIST SRM 981 used as an external standard to correct instrumental drift.

## 5. Results

### 5.1. Zircon U-Pb Geochronology

The analyzed zircons are prismatic, euhedral to subhedral, colorless, and transparent, with grain sizes ranging from 50 to 200  $\mu\text{m}$  and length-to-width ratios of 2:1 to 3:1. Cathodoluminescence (CL) images reveal clear oscillatory zoning, a characteristic feature of magmatic zircons (Figure 5). In addition to these textural features, the Th/U ratios range from 0.30 to 0.95 (except for a few inherited grains), aligning with typical magmatic Th/U values [42]. This combination of morphological characteristics, CL patterns, and Th/U ratios collectively supports the classification of these zircons as magmatic in origin. Although high-T metamorphic zircons can exhibit variable Th/U ratios, sometimes up to 3.2 [43–46], this variability generally lacks the accompanying oscillatory zoning observed here. The detailed results of the zircon U-Pb geochronology analysis are available in Supplementary Table S1.

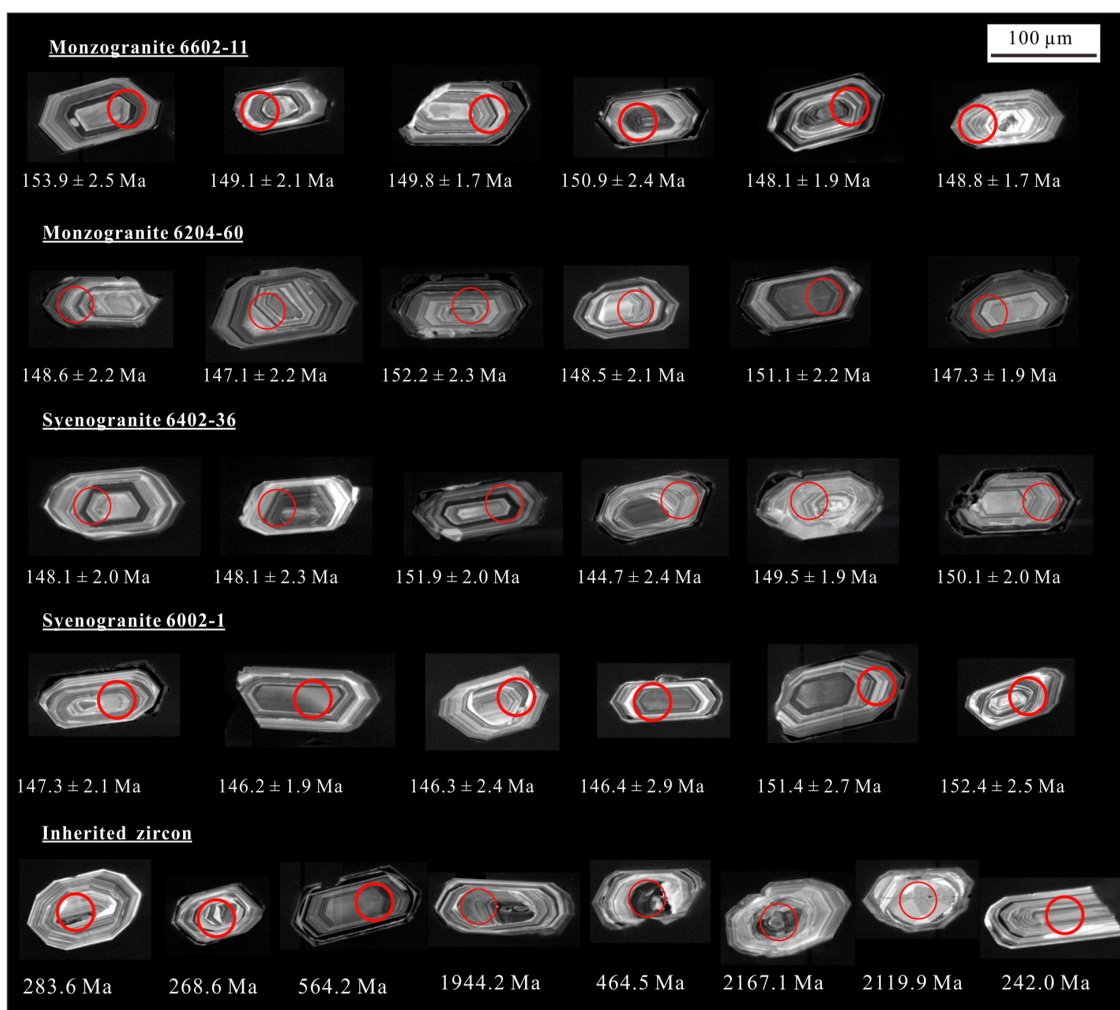


**Figure 5.** Cathodoluminescence (CL) images of zircons from the Shibaogou granite. The red circles indicate the locations of U-Pb dating analyses.



**Monzogranite:** For sample 6602-11, a total of 27 zircon grains were analyzed, with 24 spots forming a tight cluster near the Concordia line on the U-Pb Concordia diagram (Figure 6a). These 24 analyses yielded a weighted average  $^{206}\text{Pb}/^{238}\text{U}$  age of  $151.0 \pm 1.1$  Ma (MSWD = 1.6,  $1\sigma$ ), representing the crystallization age of the porphyritic monzogranite. The U, Th, and Pb contents are 854–2604 ppm, 454–1417 ppm, and 32–100 ppm, respectively. The other three spots correspond to inherited zircons, with  $^{206}\text{Pb}/^{238}\text{U}$  ages of 269 Ma, 284 Ma, and 564 Ma. For sample 6204-60, nineteen zircon grains were analyzed, with 18 spots lying near the U-Pb Concordia line (Figure 6b). The weighted mean  $^{206}\text{Pb}/^{238}\text{U}$  age is  $150.1 \pm 1.3$  Ma (MSWD = 1.7,  $1\sigma$ ), also representing the crystallization age. The U, Th, and Pb contents are 907–2062 ppm, 413–1109 ppm, and 30–78 ppm, respectively. One analyzed spot corresponds to an inherited zircon, with a  $^{207}\text{Pb}/^{206}\text{Pb}$  age of 1944 Ma (Figure 5).

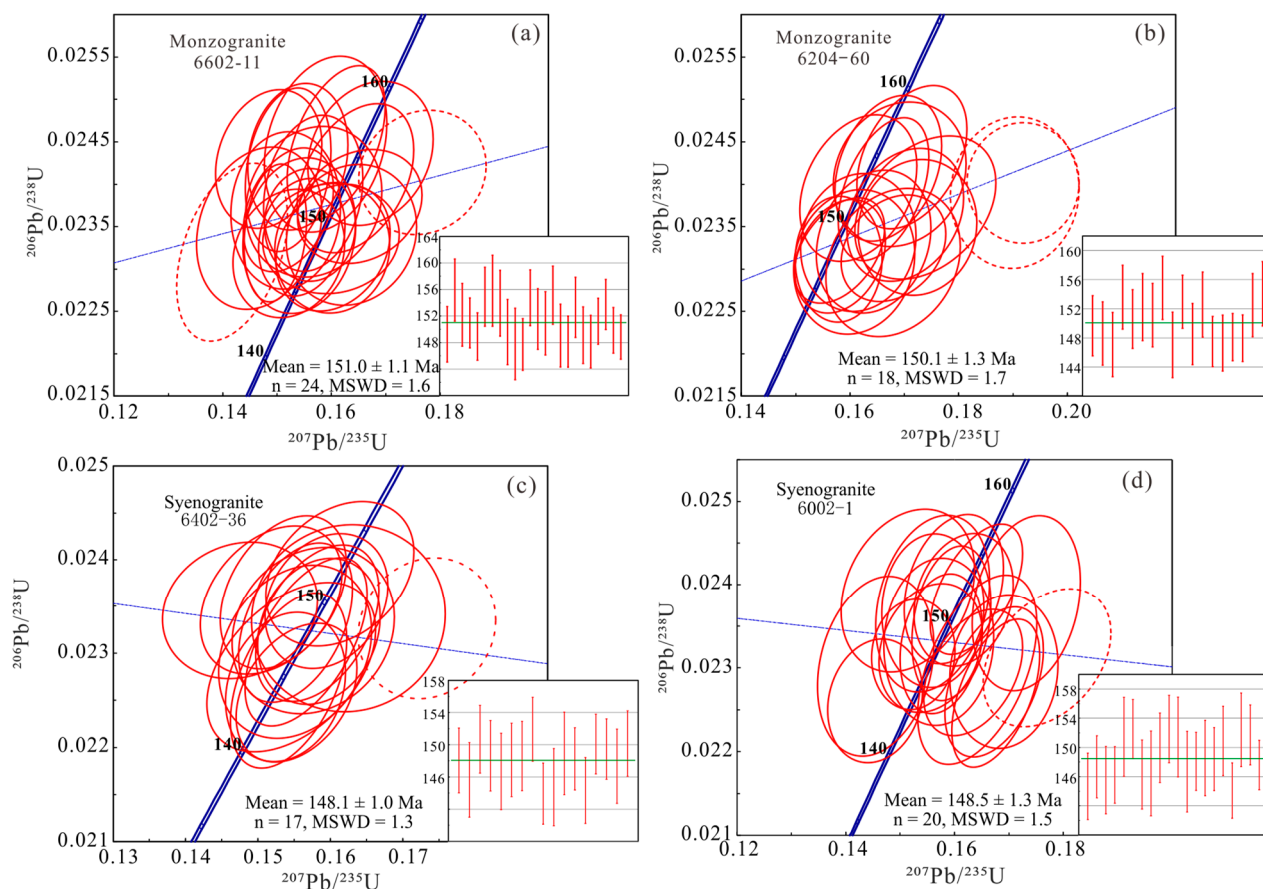


**Figure 6.** Zircon U-Pb Concordia diagram of samples from the Shibaogou granite. Monzogranite samples: (a) 6602-11, (b) 6204-60. Syenogranite samples: (c) 6402-36, (d) 6002-1.

**Syenogranite:** For sample 6402-36, a total of 20 zircon-analyzed spots were measured, with 17 spots falling on or near the U-Pb Concordia line. The weighted mean  $^{206}\text{Pb}/^{238}\text{U}$  age is  $148.1 \pm 1.0$  Ma (MSWD = 1.3,  $1\sigma$ , Figure 6c). The U, Th, and Pb contents are 660–2430 ppm, 385–1227 ppm, and 27–84 ppm, respectively. Three other spots correspond to inherited zircons, with ages of 465 Ma ( $^{206}\text{Pb}/^{238}\text{U}$  age), 2167 Ma, and 2120 Ma ( $^{207}\text{Pb}/^{206}\text{Pb}$  ages) (Figure 5). For sample 6002-1, twenty-one zircon grains were analyzed, with 20 spots located near the Concordia line on the U-Pb Concordia diagram (Figure 6d). The weighted mean  $^{206}\text{Pb}/^{238}\text{U}$  age is  $148.5 \pm 1.3$  Ma (MSWD = 1.5,  $1\sigma$ ), representing the crystallization age. The U, Th, and Pb contents are 1117–3504 ppm, 591–1771 ppm, and 39–114 ppm, respectively. One analyzed spot corresponds to an inherited zircon, with a  $^{206}\text{Pb}/^{238}\text{U}$  age of 242 Ma.

### 5.2. Major and Trace Element Geochemistry

The results of the whole-rock major and trace element analyses are shown in Table S2. There are minimal differences in the major element characteristics between the monzogranite and syenogranite. The  $\text{SiO}_2$  content ranges from 70.49 to 74.34 wt.% in the monzogranite and from 73.61 to 75.68 wt.% in the syenogranite; the  $\text{Al}_2\text{O}_3$  content is 13.09–14.08 wt.% and 12.50–13.31 wt.%, respectively; the  $\text{K}_2\text{O}$  content is 3.58–5.07 wt.% and 4.30–5.82 wt.%; the  $\text{Na}_2\text{O}$  content is 3.54–4.65 wt.% and 3.25–4.22 wt.%; the  $\text{CaO}$  content is 1.60–2.13 wt.% and 1.00–1.43 wt.%; the total iron (total  $\text{Fe}_2\text{O}_3$ ) content is 0.63–2.67 wt.% and 0.32–1.55 wt.%; and the  $\text{MgO}$  content is 0.33–0.73 wt.% and 0.23–0.48 wt.%. Generally, the studied granites have high contents of Si and K, low contents of Ca, Mg, and Fe, and are rich in alkali with  $\text{K}_2\text{O} + \text{Na}_2\text{O}$  content ranging from 7.60 to 9.07 wt.%. Syenogranites show stronger differentiation characteristics than monzogranites.

The  $\text{K}_2\text{O}/\text{Na}_2\text{O}$  ratios of monzogranite and syenogranite are 0.77–1.39 (average 1.08) and 1.08–1.79 (average 1.31), respectively. The Rittmann index ( $\delta$ ) is 1.84–2.74, indicating that both belong to the calc-alkaline series. Almost all samples fall into the high-K calc-alkaline series field in the  $\text{SiO}_2$ - $\text{K}_2\text{O}$  diagram (Figure 7a). The aluminum saturation index (ASI or A/CNK values) is 0.91–0.99 and 0.88–1.04 for the monzogranite and syenogranite, respectively. In the A/CNK-A/NK diagram, both rock types generally plot within the metaluminous range (Figure 7b). It is suggested that the ore-forming intrusions are overall high-K calc-alkaline, metaluminous granites.

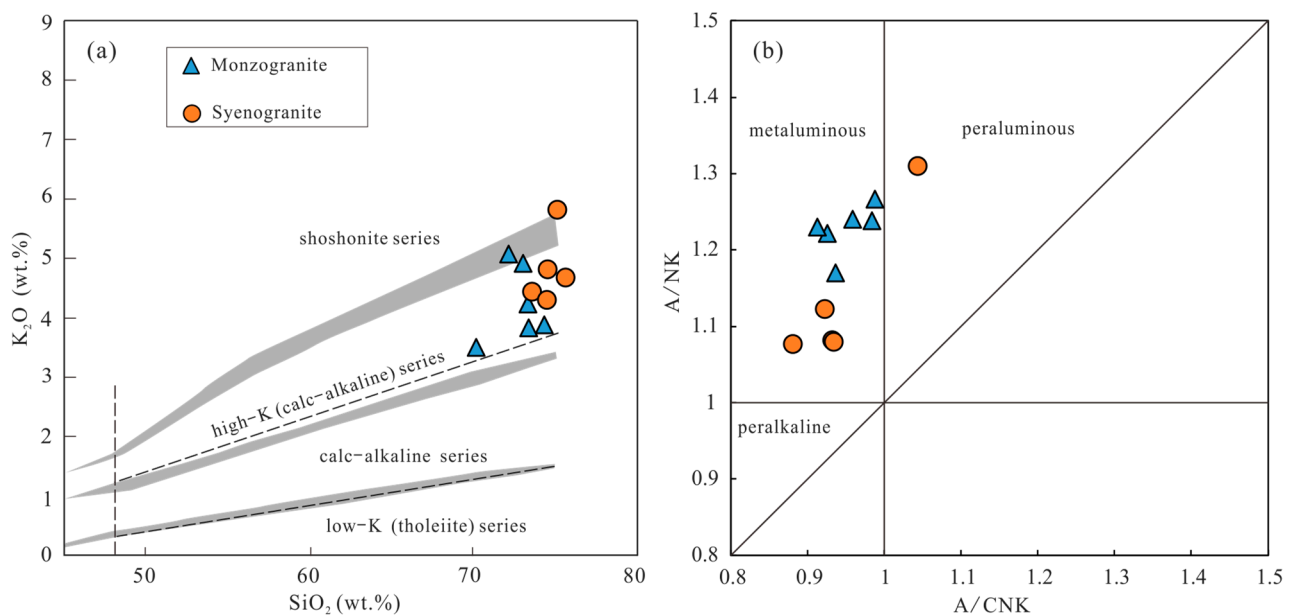


**Figure 7.** Major elements variation diagrams for the Shibaogou granite: (a)  $\text{SiO}_2$  vs.  $\text{K}_2\text{O}$  plots (base map after [47]); (b) A/NK vs. A/CNK discriminant diagram (base map after [47]).

The rare-earth elements (REEs) distribution patterns for the syenogranite and monzogranite show that both are enriched in light rare earth elements (LREE) and depleted in heavy rare earth elements (HREE). The total REEs + Y content ( $\sum\text{REEs} + \text{Y}$ ) of the monzogranite ranges from 78.65 to 258.39 ppm, showing significant fractionation between LREE and HREE (Figure 8a), with LREE/HREE ratios of 10.14–24.93 and  $(\text{La}/\text{Yb})_{\text{N}}$  ratios of 9.01–35.51. Except for sample 6602-7 ( $\delta\text{Eu} = 0.59$ , slightly deviating from the overall range), the Eu anomaly of the remaining samples is not significant, ranging from weak negative to weak positive anomalies ( $\delta\text{Eu} = 0.81$ –1.11). The syenogranite shows  $\sum\text{REEs} + \text{Y}$  values ranging from 77.48 to 126.41 ppm, with LREE/HREE ratios of 14.59–17.61 and  $(\text{La}/\text{Yb})_{\text{N}}$  ratios of 12.66–18.29 (Figure 8c), displaying moderate to weak negative Eu anomalies ( $\delta\text{Eu} = 0.69$ –0.87). Compared to the monzogranite, the fractionation between

LREE and HREE is slightly weaker, and the negative Eu anomaly is slightly stronger in the syenogranite.

The chondrite-normalized REE profiles of the Shibaogou intrusion reveal distinct zigzag patterns, suggesting a potential partial or incomplete tetrad effect. According to the method provided by Monecke [48], the REEs of the Shibaogou intrusion were divided into three groups:  $T_1$  (La, Ce, Pr, Nd),  $T_2$  (Gd, Tb, Dy, Ho), and  $T_3$  (Er, Tm, Yb, Lu). The tetrad effect values were quantitatively calculated, and the results are listed in Table S3 and Figure 8. The results show that the  $T$  values (total tetrad effect) of the REEs in the Shibaogou intrusion range from 0.063 to 0.165, indicating the presence of the tetrad effect, which is stronger in the syenogranite ( $T = 0.129$ – $0.165$ , average 0.141) than that in the monzogranite ( $T = 0.063$ – $0.144$ , average 0.102). The  $T_1$  values range from 0.037 to 0.188, with an average of 0.129, predominantly exhibiting the M-type and W-type composite tetrad effect of both type granites. The  $T_2$  values range from 0.093 to 0.180, with an average of 0.131, mainly showing a W-type tetrad effect. The  $T_3$  values range from 0.024 to 0.161, with an average of 0.072, and this group generally shows a weak M-type tetrad effect.

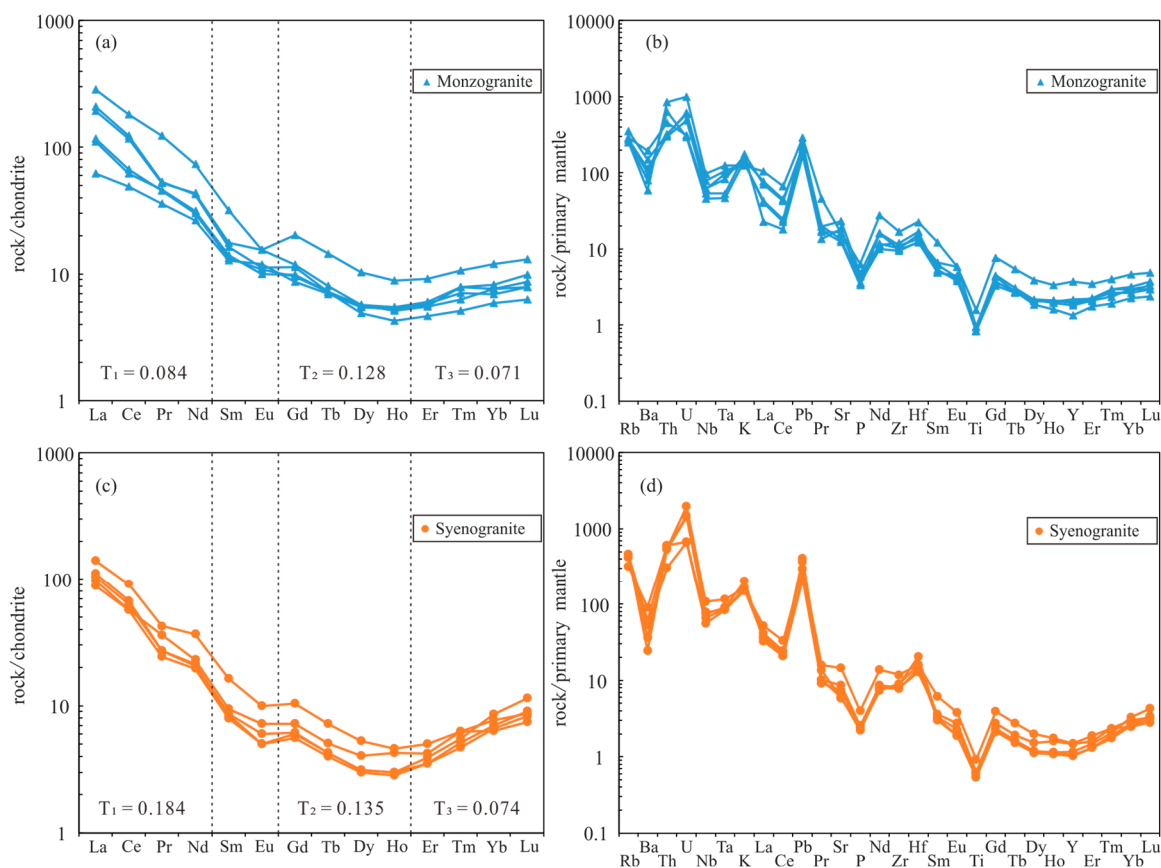


**Figure 8.** Chondrite-normalized REE patterns ((a,c), normalized values are from [49]) and primitive mantle-normalized trace element patterns ((b,d), normalized values are from [50]) for the Shibaogou granite.

The trace element characteristics of both rock types are similar, with enrichment in crustal-affinity elements such as Rb, U, Th, Pb, and K, and depletion in Nb, Ta, Ti, Ba, and P (Figure 8b,d). The Mo and W contents of the Shibaogou intrusion are 0.34–6.95 ppm (average 2.38 ppm) and 0.52–7.89 ppm (average 2.24 ppm), respectively, which are generally higher than the average values for the continental crust (0.8 ppm and 1 ppm [51]).

Monzogranite sample 6602-7 is located near the contact zone with the wallrocks and is strongly influenced by alteration and wall-rock interactions, resulting in higher contents of minerals like titanite and epidote compared to other samples (Figure 4d).

Consequently, this sample also has higher contents of  $\Sigma$ REEs, Ti, Fe, and Y. The strong negative Eu anomaly in this sample may be related to the intense sericitization it has undergone (Figure 4d), a process known to significantly enhance the negative Eu anomaly in whole-rock compositions [52].

Samples 6204-49 and 6002-2 exhibit notably higher K<sub>2</sub>O (5.07 wt.% and 4.92 wt.%, respectively), Ba (1285 ppm and 992 ppm, respectively), and Rb (175 ppm and 210 ppm, respectively) contents compared to the average values observed in other monzogranite samples (3.88%, 577 ppm, and 159 ppm, respectively; see Table S2). This enrichment suggests that these samples have undergone more intense K-feldspar alteration, as confirmed by petrographic observations (Figure 4e,f). This alteration may explain the weak positive Eu anomaly in these samples, given that K-feldspar is typically enriched in Eu. Although these samples exhibit elevated Mo and W concentrations (6.95 ppm and 0.6 ppm for 6204-49, respectively; 6.85 ppm and 7.89 ppm for 6002-2, respectively), correlation analysis (see Supplementary Figure S1) shows no consistent relationship between K<sub>2</sub>O, Ba, Rb, and Mo, W levels, indicating that the Mo and W enrichment may result from other geochemical processes or mineralogical factors within the syenogranite and monzogranite.

### 5.3. Whole-Rock Sr-Nd-Pb Isotopes

This study obtained 11 sets of Sr-Nd isotope data. The <sup>87</sup>Sr/<sup>86</sup>Sr ratios range from 0.710084 to 0.720695, and <sup>143</sup>Nd/<sup>144</sup>Nd ratios range from 0.511734 to 0.511864, with relatively small variations in the results (Table S4). The isotope compositions for the monzogranite and syenogranite were recalculated based on the crystallization ages of 150 Ma and 148 Ma, respectively. The initial <sup>87</sup>Sr/<sup>86</sup>Sr ratios (*I*<sub>Sr</sub>) of the monzogranite range from 0.707051 to 0.708989, with  $\epsilon_{\text{Nd}}(t)$  values ranging from  $-15.33$  to  $-13.17$ , and the two-stage Nd model ages (*T*<sub>DM2</sub>) range from 2.01 Ga to 2.19 Ga. For the syenogranite, the *I*<sub>Sr</sub> values range from 0.706456 to 0.708062, with  $\epsilon_{\text{Nd}}(t)$  values ranging from  $-14.04$  to  $-13.24$ , and *T*<sub>DM2</sub> ranging from 2.01 Ga to 2.08 Ga. These results are consistent with those reported by Jin [53] for the Shibaogou intrusion, with the *I*<sub>Sr</sub> of 0.70723–0.70931,  $\epsilon_{\text{Nd}}(t)$  of  $-19.25$  to  $-11.68$ , and *T*<sub>DM2</sub> of 1.9 Ga and 2.5 Ga.

This study also obtained 11 sets of whole-rock Pb isotope data for the Shibaogou intrusion (Table S5), with 17.885–19.220 of <sup>206</sup>Pb/<sup>204</sup>Pb, 15.496–15.617 of <sup>207</sup>Pb/<sup>204</sup>Pb, and 38.415–38.897 of <sup>208</sup>Pb/<sup>204</sup>Pb. Based on the Pb isotope ratios; U-Pb ages; and U, Th, and Pb contents, the Pb isotope ratios were recalculated to the time of intrusion emplacing. For the monzogranite, the (<sup>206</sup>Pb/<sup>204</sup>Pb)<sub>t</sub> ranges from 17.347 to 17.589, (<sup>207</sup>Pb/<sup>204</sup>Pb)<sub>t</sub> ranges from 15.479 to 15.594, and (<sup>208</sup>Pb/<sup>204</sup>Pb)<sub>t</sub> ranges from 37.996 to 38.411, with average values of 17.506, 15.506, and 38.149, respectively. For the syenogranite, the (<sup>206</sup>Pb/<sup>204</sup>Pb)<sub>t</sub> ranges from 17.440 to 17.614, (<sup>207</sup>Pb/<sup>204</sup>Pb)<sub>t</sub> ranges from 15.477 to 15.496, and (<sup>208</sup>Pb/<sup>204</sup>Pb)<sub>t</sub> ranges from 37.998 to 38.276, with average values of 17.531, 15.486, and 38.078, respectively. In the <sup>208</sup>Pb/<sup>204</sup>Pb vs. <sup>206</sup>Pb/<sup>204</sup>Pb diagram, the samples fall near the lower crust evolution line; in the <sup>207</sup>Pb/<sup>204</sup>Pb vs. <sup>206</sup>Pb/<sup>204</sup>Pb diagram, the samples fall near the orogenic belt evolution line (Figure 9) [54].



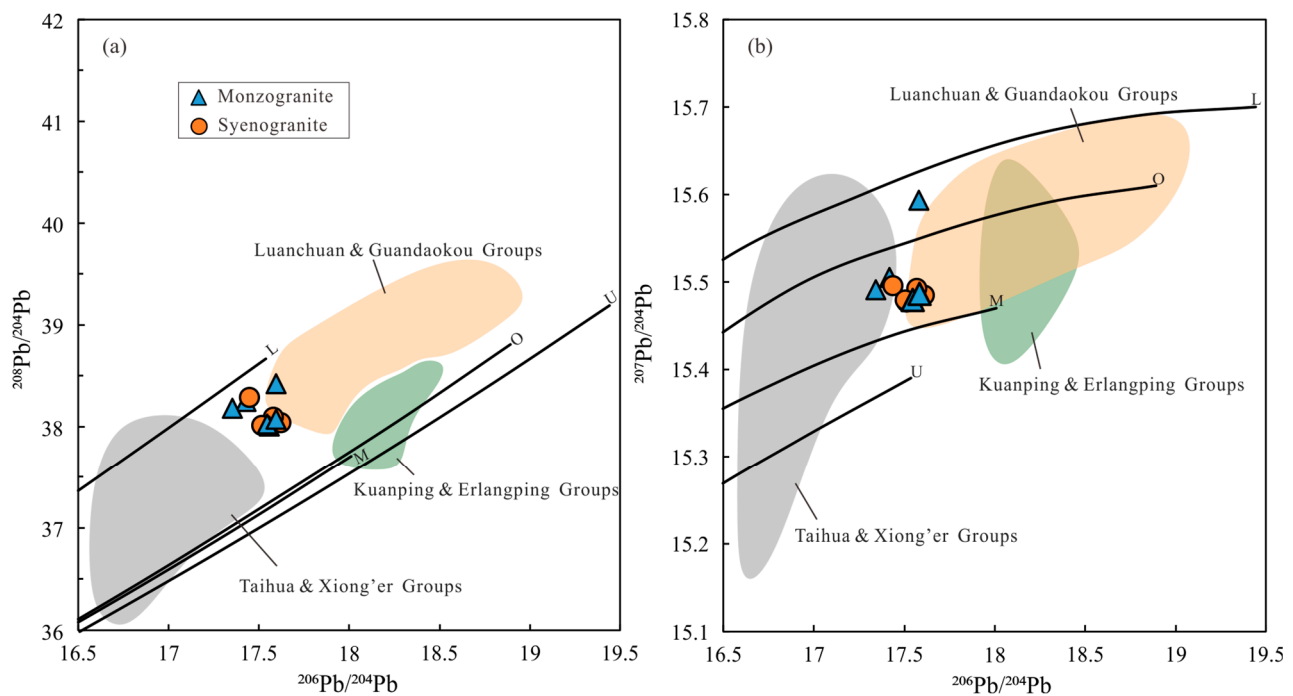


**Figure 9.** Whole-rock lead isotopic composition diagram of Shibaogou granite. (a)  $^{208}\text{Pb}/^{204}\text{Pb}$  vs.  $^{206}\text{Pb}/^{204}\text{Pb}$  diagram; (b)  $^{207}\text{Pb}/^{204}\text{Pb}$  vs.  $^{206}\text{Pb}/^{204}\text{Pb}$  diagram. The Pb isotope of strata has been recalculated to 150 Ma, and the initial data are from Taihua and Xiong'er Group [55–58], Luanchuan and Guandaokou Group [59], and Kuanping and Erlangping Group [60]. The trends for U (upper crust), O (orogenic belt), M (mantle), and L (lower crust) are from [54].

## 6. Discussion

### 6.1. Categorization of the Shibaogou Granite

The Shibaogou intrusion is a composite pluton, primarily composed of porphyritic monzogranite and porphyritic syenogranite, locally including mafic enclaves [19]. The characteristics of mineralogy and geochemistry of the Shibaogou granites are consistent with the KCG-type (K-rich and K-feldspar porphyritic calc-alkaline) granitoids defined by Barbarin [61]. This type of granite typically forms during the tectonic transition period in continental collision, reflecting crustal remelting processes [61,62]. In the (Y + Nb)-Rb tectonic diagram, the samples fall into the post-collision granites zone and near the syn-collision granites zone ([63] Figure 10a). The trend from monzogranite to syenogranite is consistent with the trend of continent–continent collision in the Rb-(Y + Nb) diagram, suggesting these granites are closely related to the collisional orogeny [63]. In the Hf-Rb/30-Ta  $\times$  3 diagram, the samples fall within the late- to post-collision granites field ([64] Figure 10b).

The origin of the biotite-bearing granitoids, including the Shibaogou granite, remains complex due to the absence of diagnostic amphibole for I-type and cordierite for S-type granites [22]. The  $I_{\text{Sr}}$  values range from 0.7065 to 0.7090 (average 0.70746), indicating a significant contribution from an older crustal source. The ASI values (0.88 to 1.04) are typical of I-type granites, yet the  $\text{K}_2\text{O}/\text{Na}_2\text{O}$  ratios (0.77 to 1.79) and low  $\epsilon_{\text{Nd}}(t)$  values (−15.33 to −13.17) suggest an involvement of deeper crustal materials, often associated with S-type characteristics [65,66]. This combination of features likely reflects a mixed or complex source [22]. Additionally, Pb isotopic data support a lower crustal origin. Together, these characteristics align with collision-type granites, as defined by Chen [65], suggesting formation during a collisional orogenic event.

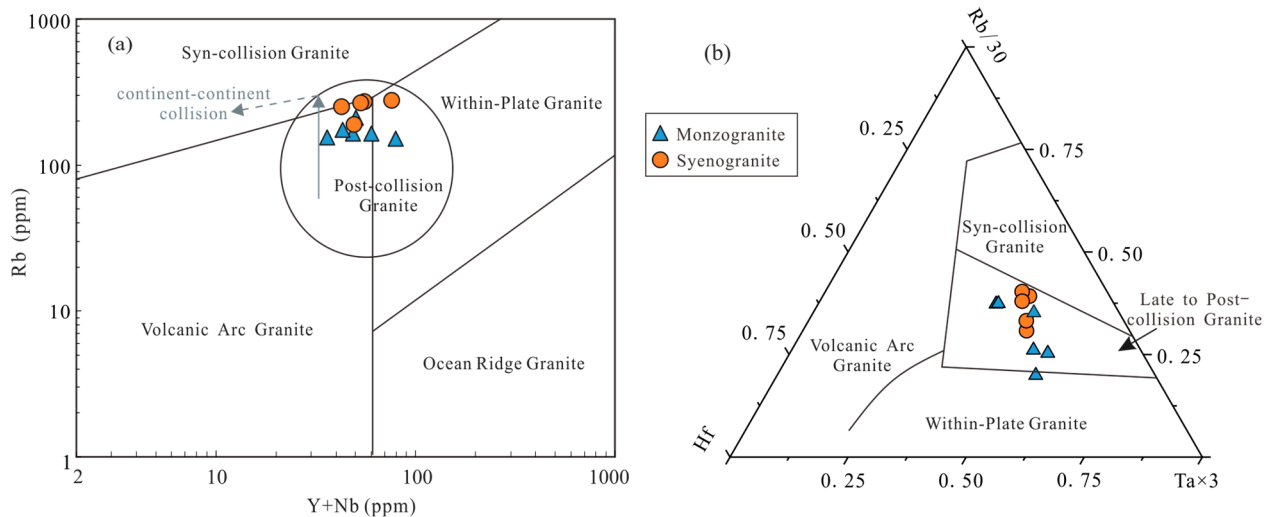


**Figure 10.** Discriminant diagrams for tectonic environment of Shibaogou granite. (a) Granite (Y + Nb)-Rb tectonic diagram (base map from [63]). (b) Granite Hf-Rb/30-Ta  $\times$  3 tectonic diagram (base map from [64]).

### 6.2. Tectonic Characteristics of the Magmatic Source

The Shibaogou intrusion exhibits low Sr, low Y (Yb), and high Sr/Y (Yb) characteristics, which are generally considered indicative of partial melting of the thickened lower crust [67]. This study employed the Sr/Y ratio and  $(La/Yb)_N$  ratio method to quantitatively estimate the depth of the magma source region. The formulas used for the calculation are as follows [68]:  $D_{Sr/Y} = 0.67Sr/Y + 28.21$ ,  $D_{La/Yb} = 27.78 \ln [0.34(La/Yb)_N]$ , where D represents the source region depth (in km). The calculated results show that the source depths are 41–51 km and 41–69 km, with average values of 51 km and 48 km, respectively (excluding the strongly altered sample, Table S2). The depths significantly exceed the normal thickness of continental crust ( $\sim 35$  km), confirming that the magma source is located in the thickened lower crust. This finding is consistent with the tectonic background of the Qinling Orogen, which experienced intense compression and crustal thickening during the Mesozoic [6,69].

The REE patterns of the Shibaogou intrusion provide important insights into the residual mineral assemblage in the magmatic source, as the studied granites conform to a partial melting model with minimal influence from fractional crystallization (Figure 11a [70,71]). The intrusion is generally enriched in LREE and depleted in HREE, with high  $(La/Lu)_N$  ratios (7.9–33.2, 15.7 on average, Table S2) and low  $Yb_N$  and  $Lu_N$  values (mainly  $< 10$ , Table S3), suggesting the presence of garnet as a residual phase in the magmatic source [72–74]. Although there are Gd–Er convex profiles in the normalized REEs pattern of syenogranites (Figure 8c), this does not suggest that the amphibole is a dominant residual in the magmatic source, as the depletion of Gd–Er is not significant in the earlier monzogranites (Figure 8a). The monzogranite in Shibaogou pluton is more representative of the characteristics of initial magma than the syenogranite. Therefore, there may be a small amount of amphibole residual in the magmatic source, but it is not the main residual phase. In the La-La/Sm diagram, a fractional crystallization trend is observed from monzogranite to late-stage syenogranite, corresponding to the stronger evolution characteristic of the syenogranite. However, the Sr-Ba diagram does not show the fractional trend of amphibole (Figure 11b, [71]). Therefore, the apparent Gd–Er depletion observed in the syenogranite may be related to the early crystallization of other Gd–Er-rich accessory minerals, such as titanite and apatite [75,76]. The REEs tetrad effect indicates the enrichment of volatile components (such as F, Cl, and  $H_2O$ ) during the magmatic differentiation process, suggesting that apatite may be the primary early fractional phase [75].

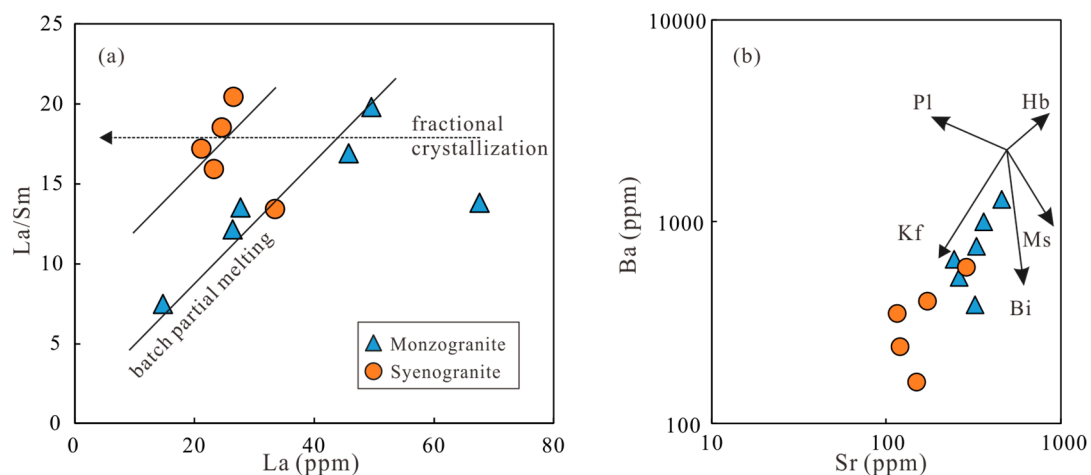


**Figure 11.** (a) La/Sm vs. La plot shows a batch partial melting trend [70]; (b) Ba vs. Sr plot shows the trend of mineral fractionation phase (arrow direction are after Rollinson [71]), ruling out the influence from the fractionation of plagioclase and hornblende. Bi = biotite, Hb = hornblende, Kf = K-feldspar, Ms = muscovite, Pl = plagioclase.

Although the Shibaogou intrusion has a relatively low Sr content, the absence of a significant negative Eu anomaly suggests that plagioclase was not a residual phase in the magma source, and plagioclase did not undergo significant fractional crystallization (Figure 11b) [77,78]. Additionally, the high magmatic oxygen fugacity ( $\Delta\text{FMQ} +1.25$  to  $+3.56$ , calculated by Yang [20]) indicates that Eu primarily existed as  $\text{Eu}^{3+}$ , reducing the likelihood of a pronounced Eu anomaly due to the low compatibility of  $\text{Eu}^{3+}$  in plagioclase. In terms of trace elements, characteristics of the depletion of Nb, Ta, Ti, and the high Nb/Ta ratios (11.2–17.9, 14.6 on average) indicate the presence of Ti-Fe oxides (such as rutile) as residual phases, further supporting the high-pressure characteristics of the source region [79].

In summary, this study suggests that the residual mineral assemblage in the magmatic source of the Shibaogou intrusion consists of garnet + rutile  $\pm$  amphibole, similar to the amphibolite eclogite source of adakitic rocks. This points to a high-pressure thickened lower crustal source [67]. Considering the calculated source depth (approximately 40–60 km) and assuming an average crustal density of  $2.8 \text{ g/cm}^3$ , the pressure conditions in the source region can be inferred to be around 1.1–1.65 Gpa. The stable presence of garnet and rutile typically requires pressures greater than 1.0–1.5 Gpa [79,80], consistent with the above quantitative estimation result. This pressure range corresponds to the conditions under which partial melting of the lower crust generates adakitic rocks, as demonstrated in experimental petrological studies [80,81].

### 6.3. Magma Origin

The Sr-Nd isotopic composition of the Shibaogou intrusion falls in the lower part of the fourth quadrant in the  $I_{\text{Sr}-\epsilon_{\text{Nd}}}(t)$  diagram (Figure 12), indicating that its origin is predominantly derived from ancient crustal material [82]. Potential magma source regions include the Taihua Supergroup, Xiong'er Group, Luanchuan Group–Guandaokou Group, Erlangping Group, Kuanping Group, and Qinling Group. Some researchers have also proposed contributions from the Yangtze Plate, suggesting that the Kongling and Yudongzi Groups could be potential source regions [83,84]. Based on the previous analysis, the magma is inferred to originate from depths exceeding 40 km, corresponding to the lower crust, thus ruling out the shallower crustal units, such as the Luanchuan and Guandaokou Groups, as primary magma sources.

When recalculating the Sr-Nd isotopic compositions of potential geological end-members (Taihua Supergroup, Xiong'er Group, Erlangping Group, Kuanping Group, Qinling Group, Yudongzi Group, and Kongling Group) to  $t = 150 \text{ Ma}$ , a wide variation range

is observed. As shown in Figure 12, the Taihua Supergroup, Xiong'er Group, Yudongzi Group, and Kongling Group all fall within the range of ancient crustal material, making them the primary magma sources for the Shibaogou intrusion. However, geophysical models show that the Qinling Orogen underwent complex nappe structures during the Mesozoic collision between the Yangtze Plate and the North China Craton [6,85]. The Luanchuan Fault served as an intracontinental subduction zone, with the North Qinling crust subducting along the Luanchuan Fault, while the Huaxiong Block was thrust upward. These units wedged into each other in the middle-lower crust [59,85]. Since the Yudongzi and Kongling Groups are mainly distributed in the western section of the South Qinling and the northwestern area of the Yangtze Craton and are not present in the North Qinling Accretion Belt, it is unlikely that basement rocks from the Yangtze Plate contributed significantly to the magma source of the Shibaogou intrusion.

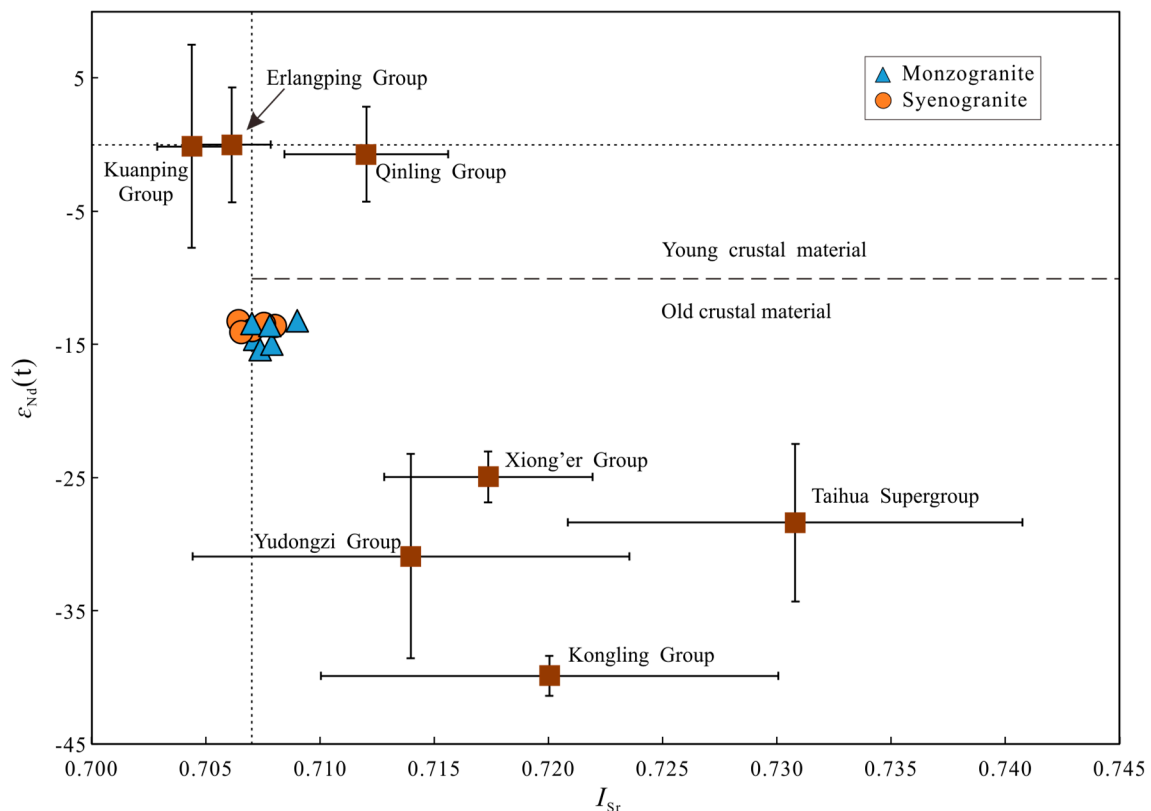


**Figure 12.** The  $I_{Sr}$ - $\epsilon_{Nd}(t)$  diagram of Shibaogou granite ( $t = 150$  Ma). The Sr-Nd isotope of strata has been recalculated to 150 Ma, and the initial data are from the Taihua Supergroup [57,86,87], Xiong'er Group [58,88,89], Qinling Group [90], Kuanping Group and Erlangping Group [60], Yudongzi Group, and Kongling Group [84,91].

The Taihua Supergroup, forming the crystalline basement of the Huaxiong Block, is consistent with previous analyses suggesting a magmatic origin derived from lower crust remelting, making it an ideal magma source for the Shibaogou intrusion. The  $T_{DM2}(Nd)$  ages ( $\sim 2.1$  Ga) and inherited zircon ages (1.9 to 2.2 Ga) of the Shibaogou intrusion are consistent with the formation ages of both the Taihua Supergroup and the Xiong'er Group. However, the Xiong'er Group and Taihua Supergroup exhibit relatively higher  $^{87}Sr/^{86}Sr$  ratios (averages values of 0.71736 and 0.71888 for the Xiong'er Group and the Taihua Supergroup at  $t = 150$  Ma, respectively) and lower  $\epsilon_{Nd}(t)$  values (averages values of  $-24.93$  and  $-28.36$  for the Xiong'er Group and the Taihua Supergroup, respectively). This suggests the need for a mixing end-member with lower  $^{87}Sr/^{86}Sr$  and higher  $\epsilon_{Nd}(t)$  values to reconcile the isotopic composition of the Shibaogou granite. Whole-rock Pb isotopes indicate that a



high-radiogenic Pb isotope end-member is required to mix with the Taihua Supergroup and Xiong'er Group (Figure 9).

According to the Sr-Nd isotopic mixing model by DePaolo [82], the younger crustal rocks from the Kuanping Group and Erlangping Group in the North Qinling are ideal mixing end-members (Figure 12). Both groups exhibit low  $^{87}\text{Sr}/^{86}\text{Sr}$  ratios (average values of 0.70438 and 0.70614 for the Kuanping Group and Erlangping Group, respectively) and relatively higher  $\epsilon_{\text{Nd}}(t)$  values (average values of  $-0.11$  and  $-0.70$  for the Kuanping Group and Erlangping Group, respectively), while the higher  $^{87}\text{Sr}/^{86}\text{Sr}$  ratios observed in the Qinling Group suggest that it is not a significant mixing end-member.

Previous zircon Hf isotopic studies on the Shibaogou intrusion have shown  $\epsilon_{\text{Hf}}(t)$  values ranging from  $-28$  to  $-11$ , higher than those of the Taihua Supergroup and Xiong'er Group ( $\epsilon_{\text{Hf}}(t)$  values ranging from  $-35$  to  $-25$ ). The North Qinling juvenile crustal rocks (in the Kuanping Group and Erlangping Group) provide a suitable high  $\epsilon_{\text{Hf}}(t)$  end-member (Figure 13). In addition, the  $\epsilon_{\text{Hf}}(t)$  values of the inherited zircons (1.5–2.5 Ga) are consistent with the Hf isotopic compositions of these end-members (Figure 13), further confirming that these geological units are the main sources of the Shibaogou intrusion.

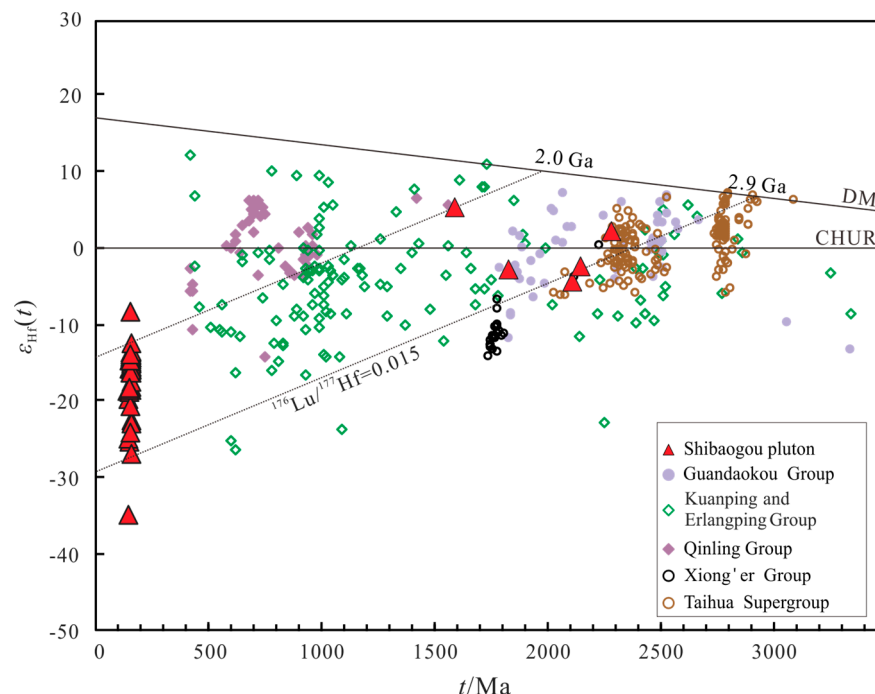


**Figure 13.** Zircon Hf isotopic diagram of Shibaogou granite ( $t = 150$  Ma). Data on Shibaogou granite are from Table S6. Data of strata are from the Guandaokou Group [92], Kuanping and Erlangping Group (the crustal material of North Qinling) [92,93], Qinling Group [93], Xiong'er Group [89,94], and Taihua Supergroup [26,95–97].

Although mantle-derived material could potentially provide a low  $^{87}\text{Sr}/^{86}\text{Sr}$ , high  $\epsilon_{\text{Nd}}(t)$ , and high  $\epsilon_{\text{Hf}}(t)$  end-member [11,53], there are no Yanshanian basic rocks being observed in the eastern Qinling. The mafic enclaves in the Shibaogou intrusion have consistent Sr-Nd isotopic compositions ( $t = 150$  Ma,  $I_{\text{Sr}}$ : 0.70718 to 0.70843, 0.70761 on average;  $\epsilon_{\text{Nd}}(t)$ :  $-15.20$  to  $-11.62$ ,  $-13.45$  on average [53]) with its host, suggesting that they are more likely to be cumulate enclaves of the same source rather than products of mixing with mantle-derived mafic magma [98]. The geochemical characteristics of the Shibaogou intrusion show high  $\text{SiO}_2$  contents ( $>70\%$ ) and enrichment in large ion lithophile elements, Pb, and LREE, while high field strength elements and HREE are depleted, indicating a typical continental crust origin [6,22,65]. Although the Nb/Ta ratios have been increased by the rutile or other Fe-Ti oxide as residual in the source, most of the values (mainly 11–16, with 14.6 on average) are lower than a typical mantle-derived feature

of ~17.5, aligning with the crustal origin [99]. The very low Ni (1.9–4.0 ppm, 2.9 ppm on average) and V (5.1–29 ppm, 13 ppm on average) contents of the studied granites also rule out the involvement of any significant mantle material [22]. Furthermore, geophysical data show that major faults in the region, such as the Luanchuan Fault, are obviously shallower than the Moho discontinuity, indicating that the Mesozoic magmatic rocks in this area are unlikely to have originated predominantly from the mantle [59].

6.4. Tectonic Setting and Metallogenic Significance

The Indosinian movement at the end of the Triassic in the Qinling Orogen was characterized by the subduction, consumption, and eventual closure of the Paleo-Tethys Ocean (around 200 Ma), followed by the convergence and collision between the Yangtze Plate and the Qinling-North China Craton along the Mianlve suture zone (195–155 Ma). After 155 Ma, the tectonic regime gradually shifted from compression to extension, eventually transitioning into an extensional setting after 130 Ma [6,21,22,100–102]. The Shibaogou intrusion, which emplaced around 150 Ma, occurred approximately 50 Ma after the closure of the Paleo-Tethys Ocean, during the compressional-extensional transitional environment of the collisional orogeny (Figure 14). The magma was derived from partial melting of the thickened lower crust, consistent with crustal shortening and vertical thickening caused by continental collision. The primary magma source included the crystalline basement of the Taihua Supergroup and the overlying Xiong'er Group of the Huaxiong Block, as well as the Kuanping Group and Erlangping Group from the North Qinling Accretion Belt (Figure 14). This origin aligns with the “lateral sources” concept in the CMF model, suggesting that some of the material for magmatism and mineralization originated from the subducted continental crust [103].

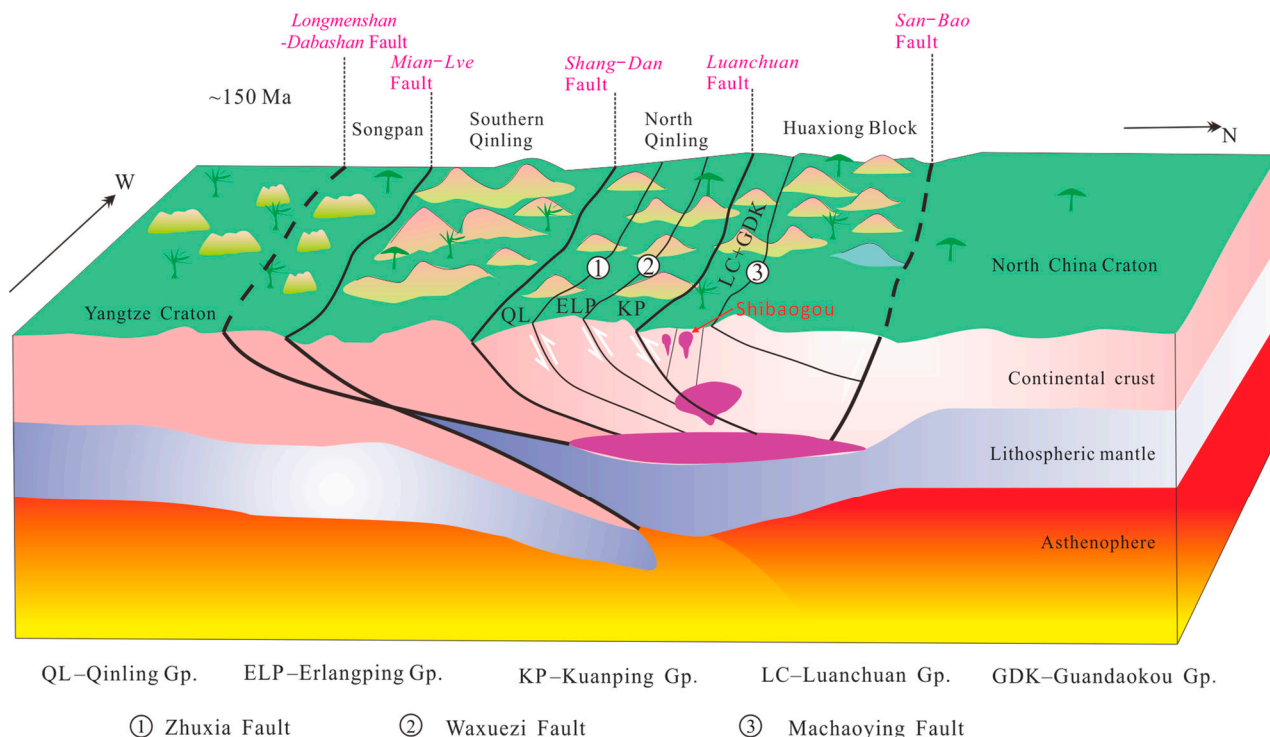


Figure 14. Yanshanian tectonic model of Qinling orogen and genesis model of the Shibaogou pluton (modified after [9]).

During the compressional-extensional transition period of the collisional orogeny, partial melting occurred in the middle-lower crust of the Huaxiong Block (Taihua Supergroup and Xiong'er Group) and the subducted North Qinling (Kuanping and Erlangping Groups), under conditions of increasing temperature and decompression. The resulting magma

gradually coalesced to form a magma chamber, which was emplaced multiple times between 151 and 148 Ma, ultimately forming the Shibaogou intrusion (Figure 14). The zircon U-Pb ages of the Shibaogou intrusion cluster between 151 and 148 Ma, aligning with previous results: Bao [15] reported a SHRIMP zircon U-Pb age of  $147.2 \pm 1.7$  Ma, Zhang [14] obtained LA-ICP-MS zircon U-Pb ages ranging from  $149.1 \pm 0.8$  Ma to  $147.4 \pm 0.8$  Ma, and Yang [20] reported LA-ICP-MS zircon U-Pb ages of  $147.0 \pm 1.0$  Ma to  $146.9 \pm 1.1$  Ma. These ages suggest that the magmatic activity of the Shibaogou intrusion was concentrated between 151 and 146 Ma, with multiple emplacement events. Previous Re-Os isotopic dating of molybdenite from the Shibaogou deposit shows ages between 151.2 Ma and 146.3 Ma [104], indicating that the mineralization closely matches the intrusion age, confirming a genetic link. The presence of REEs tetrad effect of the Shibaogou intrusion indicates the high differentiation characteristics of the magma, forming residual melts enriched in F, Cl, and water [48,105]. The process created a fluid-melt coexistence system and resulted in significant fluid-melt interactions [48,105], greatly facilitating the mineralization of W and Mo. The overlap between the emplacement age and mineralization age also suggests that in the late stage of magmatic activity, magmatic and metallogenic processes occurred synchronously.

Based on these chronology results, the magmatic-hydrothermal activity at the Shibaogou deposit lasted for approximately 5 million years. This duration is comparable to other well-known magmatic-hydrothermal systems globally, such as the Chuquicamata deposit in Chile and the Butte deposit in Montana, USA, where activity persisted for 3–5 million years [106–108]. These examples suggest that prolonged, multi-stage magmatic-hydrothermal activity is crucial for the formation of large deposits. In addition, high oxygen fugacity ( $fO_2$ ) conditions likely influenced the mobility and deposition of W and Mo in the Shibaogou intrusion. Under oxidizing conditions, W and Mo become more soluble in magmatic-hydrothermal fluids, enhancing their transport and concentration in mineralized zones [109]. This oxidizing environment may thus contribute to the observed W and Mo mineralization.

## 7. Conclusions

1. The ore-causative lithology of the Shibaogou intrusion consists of porphyritic biotite monzogranite and porphyritic biotite syenogranite, with characteristics of both S-type and I-type granites.
2. Zircon U-Pb dating indicates an emplacement age of approximately 151–148 Ma, corresponding to the compressional–extensional transition in the collisional orogeny between the Yangtze Plate and the North China Craton.
3. Geochemical data suggest a significant continental crust origin, with garnet and rutile as residual phases, indicating that the magma was derived from partial melting of thickened lower crust at depths of 40–60 km.
4. Sr-Nd-Pb isotopic analyses reveal a mixed source, primarily from the Taihua and Xiong'er Groups of the Huaxiong Block, with contributions from juvenile crustal rocks in the Kuanping and Erlangping Groups of the North Qinling Accretion Belt.
5. The Shibaogou deposit underwent prolonged magmatic-hydrothermal activity lasting approximately 5 million years. Elevated oxygen fugacity conditions facilitated the mineralization of W and Mo, similar to other large hydrothermal systems globally.

**Supplementary Materials:** The following supporting information can be downloaded at <https://www.mdpi.com/article/10.3390/min14111173/s1>, Figure S1: The correlation diagrams for  $K_2O$ , Ba, and Rb vs. W and Mo. Table S1: LA-ICP-MS zircon U-Pb data for the Shibaogou granite. Table S2: Major (wt.%) and trace elements (ppm) of Shibaogou granite. Table S3: REEs tetrad effect calculation results of Shibaogou granite [48]. Table S4: Whole-rock Sr-Nd isotopic compositions of the Shibaogou granite. Table S5: Whole-rock Pb isotopic compositions of the Shibaogou granite. Table S6: Zircon Hf isotopic compositions of the Shibaogou granite [14,15,19].

**Author Contributions:** Conceptualization, Z.Q., Z.Z. and Y.C.; investigation, Z.Q., P.H., J.Y. and Y.F.; methodology, Z.Q., N.Q. and P.H.; resources, Y.F.; writing—original draft, Z.Q., Z.Z. and N.Q.; writing—review and editing, Z.Z. and Y.C. All authors have read and agreed to the published version of the manuscript.

**Funding:** This work was funded by the National Natural Science Foundation of China (No. U2244206, 42202073, 41630313), and China Scholarship Council (202304180004).

**Data Availability Statement:** All data generated or analyzed are included within this study and its Supplementary Materials.

**Acknowledgments:** We thank Henan Xinchuan Mining Ltd. for the support in fieldwork. We are grateful to Xinkai Chen, Shen Han, and Rongzhen Tang for their discussions with us. The valuable comments and suggestions from the three reviewers considerably improved the manuscript.

**Conflicts of Interest:** Yantao Feng is an employee of Henan Xiangyan Mining Ltd. The paper reflects the views of the scientists and not the company.

## References

1. White, W.H.; Bookstrom, A.A.; Kamilli, R.J.; Ganster, M.W.; Smith, R.P.; Ranta, D.E.; Steininger, R.C. Character and origin of Climax-type molybdenum deposits. *Econ. Geol.* **1981**, *75*, 270–316.
2. Shannon, J.R.; Nelson, E.P.; Smith, R.P. Climax porphyry molybdenum deposit, Colorado: A summary. *Econ. Geol. Bull. Soc. Econ. Geol.* **2006**, *38*, 5–22.
3. Taylor, R.D.; Hammarstrom, J.M.; Piatak, N.M.; Seal, R.R. Arc-related porphyry molybdenum deposit model. *Sci. Investig. Rep.* **2012**, *2010*, 1–64.
4. Carten, R.B.; White, W.H.; Stein, H.J. High-grade granite-related molybdenum systems: Classification and origin. *Geol. Assoc. Can.* **1993**, *40*, 521–554.
5. Chen, Y.J.; Li, N. Nature of ore-fluids of intracontinental intrusion-related hypothermal deposits and its difference from those in island arcs. *Acta Petrol. Sin.* **2009**, *25*, 2477–2508. (In Chinese with English Abstract)
6. Chen, Y.J.; Franco, P.; Li, N.; Deng, X.H.; Yang, Y.F. *Geology and Geochemistry of Molybdenum Deposits in the Qinling Orogen, PR China*; Springer: Singapore, 2022; pp. 1–842.
7. Li, N.; Ulrich, T.; Chen, Y.J.; Thomsen, T.B.; Pease, V.; Pirajno, F. Fluid evolution of the Yuchiling porphyry Mo deposit, East Qinling, China. *Ore Geol. Rev.* **2012**, *48*, 442–459. [\[CrossRef\]](#)
8. Chen, Y.J.; Wang, P.; Li, N.; Yang, Y.F.; Pirajno, F. The collision-type porphyry Mo deposits in Dabie Shan, China. *Ore Geol. Rev.* **2017**, *81*, 405–430. [\[CrossRef\]](#)
9. Qi, N.; Williams-Jones, A.E.; Yu, J.; Chen, Y. The geochronology, geochemistry, and petrogenesis of the Leimengou porphyries, Qinling Orogen: A case study of intrusions associated with a Dabie-type porphyry Mo deposit. *Ore Geol. Rev.* **2023**, *163*, 105781. [\[CrossRef\]](#)
10. Yang, F.; Xue, F.; Santosh, M.; Wang, G.; Kim, S.W.; Shen, Z.; Jia, W.; Zhang, X. Late Mesozoic magmatism in the East Qinling Orogen, China and its tectonic implications. *Geosci. Front.* **2019**, *10*, 1803–1821. [\[CrossRef\]](#)
11. Wang, S.; Zhang, Y.; Zhang, H.; Zhu, A.M.; Wang, H.M.; Shi, X.F.; Ye, H.S.; Yang, Y.Q. Petrogenesis and tectonic setting of the Mesozoic Huoshenmiao intrusion in the Luanchuan ore district, Henan Province, North China. *J. Asian Earth Sci.* **2018**, *160*, 239–257. [\[CrossRef\]](#)
12. Guo, B.; Yan, C.H.; Zhang, S.T.; Han, J.W.; Yun, H.; Tan, H.Y.; Song, Q.C.; Meng, F.X. Geochemical and geological characteristics of the granitic batholith and Yuku concealed Mo-W deposit at the southern margin of the North China Craton. *Geol. J.* **2018**, *55*, 95–116. [\[CrossRef\]](#)
13. Xue, F.; Wang, G.W.; Santosh, M.; Yang, F.; Shen, Z.W.; Kong, L.; Guo, N.N.; Zhang, X.H.; Jia, W.J. Geochemistry and geochronology of ore-bearing and barren intrusions in the Luanchuan ore fields of East Qinling metallogenic belt, China: Diverse tectonic evolution and implications for mineral exploration. *J. Asian Earth Sci.* **2018**, *157*, 57–77. [\[CrossRef\]](#)
14. Zhang, Y.H.; Cao, H.W.; Xu, M.; Zhang, S.T.; Tang, L.; Wang, S.Y.; Pei, Q.M.; Cai, G.J.; Shen, T. Petrogenesis of the late Mesozoic highly fractionated I-type granites in the Luanchuan district: Implications for the tectono-magmatic evolution of eastern Qinling. *Geosci. J.* **2018**, *22*, 253–272. [\[CrossRef\]](#)
15. Bao, Z.W.; Wang, C.Y.; Zhao, T.P.; Li, C.J.; Gao, X.Y. Petrogenesis of the Mesozoic granites and Mo mineralization of the Luanchuan ore field in the East Qinling Mo mineralization belt, Central China. *Ore Geol. Rev.* **2014**, *57*, 132–153. [\[CrossRef\]](#)
16. Li, N.; Chen, Y.J.; Zhang, H.; Zhao, T.P.; Deng, X.H.; Wang, Y.; Ni, Z.Y. Molybdenum deposits in East Qinling. *Earth Sci. Front.* **2007**, *14*, 186–198. (In Chinese with English Abstract)
17. Li, Y.F.; Mao, J.W.; Hu, H.B.; Guo, B.J.; Bai, F.J. Geology, distribution, types and tectonic settings of Mesozoic molybdenum deposits in East Qinling area. *Miner. Deposits* **2005**, *24*, 292–304. (In Chinese with English Abstract)
18. Mao, J.W.; Xie, G.Q.; Pirajno, F.; Ye, H.S.; Wang, Y.B.; Li, Y.F.; Xiang, J.F.; Zhao, H.J. Late Jurassic-Early Cretaceous granitoid magmatism in Eastern Qinling, central-eastern China: SHRIMP zircon U-Pb ages and tectonic implications. *Aust. J. Earth Sci.* **2010**, *57*, 51–78. [\[CrossRef\]](#)



19. Yang, Y.; Wang, X.X.; Ke, C.H.; Li, J.B. Zircon U-Pb age, geochemistry and Hf isotopic compositions of Shibaogou granitoid pluton in the Nannihu ore district, western Henan Province. *Geol. China* **2012**, *39*, 1525–1542. (In Chinese with English Abstract)
20. Yang, Z.L.; Ren, L.; Deng, M.G.; Zhang, Z.J.; Jia, Z.; Yang, J.F.; Yang, Z.X. Pluton age and mineralogical significance of oxygen fugacity of Shibaogou Mo deposit in Luanchuan, Henan. *Nonferrous Met. (Min. Sect.)* **2023**, *75*, 134–145. (In Chinese with English Abstract)
21. Chen, Y.J.; Santosh, M. Triassic tectonics and mineral systems in the Qinling Orogen, central China. *Geol. J.* **2014**, *49*, 338–358. [[CrossRef](#)]
22. Li, N.; Chen, Y.J.; Santosh, M.; Pirajno, F. Late Mesozoic granitoids in the Qinling Orogen, Central China, and tectonic significance. *Earth-Sci. Rev.* **2018**, *182*, 141–173. [[CrossRef](#)]
23. Zhou, Z.J.; Mao, S.D.; Chen, Y.J.; Santosh, M. U-Pb ages and Lu-Hf isotopes of detrital zircons from the southern Qinling Orogen: Implications for Precambrian to Phanerozoic tectonics in central China. *Gondwana Res.* **2016**, *35*, 323–337. [[CrossRef](#)]
24. Deng, X.H.; Chen, Y.J.; Pirajno, F.; Li, N.; Yao, J.M.; Sun, Y.L. The geology and geochronology of the Waifangshan Mo-quartz vein cluster in eastern Qinling, China. *Ore Geol. Rev.* **2017**, *81*, 548–564. [[CrossRef](#)]
25. Zhang, Z.Q.; Wang, G.W.; Ma, Z.B.; Carranza, E.J.M.; Jia, W.J.; Du, J.G.; Tao, G.S.; Deng, Z.P. Batholith-stock scale exploration targeting based on multi-source geological and geophysical datasets in the Luanchuan Mo polymetallic district, China. *Ore Geol. Rev.* **2020**, *118*, 103225. [[CrossRef](#)]
26. Diwu, C.R.; Sun, Y.; Lin, C.L.; Wang, H.L. LA-(MC)-ICPMS U-Pb zircon geochronology and Lu-Hf isotope compositions of the Taihua complex on the southern margin of the North China Craton. *Chin. Sci. Bull.* **2010**, *55*, 2557–2571. [[CrossRef](#)]
27. Li, N.; Chen, Y.J.; Mcnaughton, N.J.; Ling, X.X.; Deng, X.H.; Yao, J.M.; Wu, Y.S. Formation and tectonic evolution of the khondalite series at the southern margin of the North China Craton: Geochronological constraints from a 1.85-Ga Mo deposit in the Xiong'er shan area. *Precambrian Res.* **2015**, *269*, 1–17. [[CrossRef](#)]
28. Jia, X.L.; Zhai, M.G.; Xiao, W.J.; Li, L.; Ratheesh-Kumar, R.T.; Wu, J.L.; Liu, Y. Mesoarchean to Paleoproterozoic crustal evolution of the Taihua Complex in the southern North China Craton. *Precambrian Res.* **2020**, *337*, 105451. [[CrossRef](#)]
29. He, Y.H.; Zhao, G.C.; Sun, M.; Xia, X.P. SHRIMP and LA-ICP-MS zircon geochronology of the Xiong'er volcanic rocks: Implications for the Paleo-Mesoproterozoic evolution of the southern margin of the North China Craton. *Precambrian Res.* **2009**, *168*, 213–222. [[CrossRef](#)]
30. Zhao, G.C.; He, Y.H.; Sun, M. The Xiong'er volcanic belt at the southern margin of the North China Craton: Petrographic and geochemical evidence for its outboard position in the Paleo-Mesoproterozoic Columbia Supercontinent. *Gondwana Res.* **2009**, *16*, 170–181. [[CrossRef](#)]
31. Hu, G.H.; Zhao, T.P.; Zhou, Y.Y.; Wang, S.Y. Meso-Neoproterozoic sedimentary formation in the southern margin of the North China Craton and its geological implications. *Acta Petrol. Sin.* **2013**, *29*, 2491–2507. (In Chinese with English Abstract)
32. Dong, Y.P.; Zhang, G.W.; Hauzenberger, C.; Neubauer, F.; Yang, Z.; Liu, X.M. Palaeozoic tectonics and evolutionary history of the Qinling orogen: Evidence from geochemistry and geochronology of ophiolite and related volcanic rocks. *Lithos* **2011**, *122*, 39–56. [[CrossRef](#)]
33. Cao, H.W.; Zhang, S.T.; Santosh, M.; Zheng, L.; Tang, L.; Li, D.; Zhang, X.H.; Zhang, Y.H. The Luanchuan Mo-W-Pb-Zn-Ag magmatic-hydrothermal system in the East Qinling metallogenic belt, China: Constrains on metallogenesis from C-H-O-S-Pb isotope compositions and Rb-Sr isochron ages. *J. Asian Earth Sci.* **2015**, *111*, 751–780. [[CrossRef](#)]
34. Lv, W.Q.; Liu, J.J.; Wu, F.; Zhang, H. The Geological Features and Genetic Analysis of Shibaogou Molybdenite Deposit in Luanchuan County, Henan Province. *China Molybdenum Ind.* **2014**, *38*, 20–24. (In Chinese with English Abstract)
35. He, Y.L.; Han, J.W.; Yun, H.; Hu, H.L. The discovery of a world-class tungsten and molybdenum ore deposit from deep exploration in the Luanchuan molybdenum ore concentration area, Henan Province. *Geol. China* **2020**, *47*, 1934–1936. (In Chinese)
36. Zhang, Y.Z.; Weng, J.C.; Yun, H. Geological characteristics and ore-searching prospects of the Zhuyuangou tungsten-molybdenum ore deposit. *Geol. China* **2009**, *36*, 166–173. (In Chinese with English Abstract)
37. Mao, J.W.; Xie, G.Q.; Bierlein, F.; Qü, W.J.; Du, A.D.; Ye, H.S.; Pirajno, F.; Li, H.M.; Guo, B.J.; Li, Y.F.; et al. Tectonic implications from Re-Os dating of Mesozoic molybdenum deposits in the East Qinling-Dabie orogenic belt. *Geochim. Cosmochim. Acta* **2008**, *72*, 4607–4626. [[CrossRef](#)]
38. Thompson, J.M.; Meffre, S.; Danyushevsky, L. Impact of air, laser pulse width and fluence on U-Pb dating of zircons by LA-ICPMS. *J. Anal. At. Spectrom.* **2018**, *33*, 221–230. [[CrossRef](#)]
39. Paton, C.; Woodhead, J.D.; Hellstrom, J.C.; Hergt, J.M.; Greig, A.; Maas, R. Improved laser ablation U-Pb zircon geochronology through robust downhole fractionation correction. *Geochem. Geophys. Geosyst.* **2010**, *11*, 866. [[CrossRef](#)]
40. Ludwig, K.R. *User's Manual for Isoplot 3.70: A Geochronological Toolkit for Microsoft Excel*; Berkeley Geochronology Center: Berkeley, CA, USA, 2008; pp. 1–77.
41. Yang, Y.H.; Zhang, H.F.; Chu, Z.Y.; Xie, L.W.; Wu, F.Y. Combined chemical separation of Lu, Hf, Rb, Sr, Sm and Nd from a single rock digest and precise and accurate isotope determinations of Lu-Hf, Rb-Sr and Sm-Nd isotope systems using Multi-Collector ICP-MS and TIMS. *Int. J. Mass Spectrom.* **2010**, *290*, 120–126. [[CrossRef](#)]
42. Belousova, E.; Griffin, W.; O'Reilly, S.Y.; Fisher, N. Igneous zircon: Trace element composition as an indicator of source rock type. *Contrib. Mineral. Petrol.* **2002**, *143*, 602–622. [[CrossRef](#)]
43. Vavra, G.; Schmid, R.; Gebauer, D. Internal morphology, habit and U-Th-Pb microanalysis of amphibolite-to-granulite facies zircons; geochronology of the Ivrea Zone (southern Alps). *Contrib. Mineral. Petrol.* **1999**, *134*, 380–404. [[CrossRef](#)]

44. Harley, S.L.; Carrington, D.P. The distribution of H<sub>2</sub>O between cordierite and granitic melt: H<sub>2</sub>O incorporation in cordierite and its application to high-grade metamorphism and crustal anatexis. *J. Petrol.* **2001**, *42*, 1595–1620. [[CrossRef](#)]
45. Carson, C.J.; Ague, J.J.; Grove, M.; Coath, C.D.; Harrison, T.M. U-Pb isotopic behaviour of zircon during upper-amphibolite facies fluid infiltration in the Napier Complex, East Antarctica. *Earth Planet. Sci. Lett.* **2002**, *199*, 287–310. [[CrossRef](#)]
46. Kelly, N.M.; Harley, S.L. An integrated microtextural and chemical approach to zircon geochronology: Refining the Archaean history of the Napier Complex, east Antarctica. *Contrib. Mineral. Petrol.* **2005**, *149*, 57–84. [[CrossRef](#)]
47. Maniar, P.D.; Piccoli, P.M. Tectonic discrimination of granitoids. *Geol. Soc. Am. Bull.* **1989**, *101*, 635–643. [[CrossRef](#)]
48. Monecke, T.; Kempe, U.; Monecke, J.; Sala, M.; Wolf, D. Tetrad effect in rare earth element distribution patterns; a method of quantification with application to rock and mineral samples from granite-related rare metal deposits. *Geochim. Cosmochim. Acta* **2002**, *66*, 1185–1196. [[CrossRef](#)]
49. Sun, S.S.; McDonough, W.F. Chemical and isotopic systematics of oceanic basalts: Implications for mantle composition and processes. In *Magmatism in the Ocean Basins*; Saunders, A.D., Norry, M.J., Eds.; Geological Society of London Special Publication: London, UK, 1989; Volume 42, pp. 313–345.
50. McDonough, W.F.; Sun, S.S. The composition of the Earth. *Chem. Geol.* **1995**, *120*, 223–253. [[CrossRef](#)]
51. Rudnick, R.L.; Gao, S. Composition of the Continental Crust. In *Treatise on Geochemistry*, 2nd ed.; Holland, H.D., Turekian, K.K., Eds.; Elsevier: Amsterdam, The Netherlands, 2003; Volume 4, pp. 1–51.
52. Alderton, D.H.M.; Pearce, J.A.; Potts, P.J. Rare earth element mobility during granite alteration; evidence from Southwest England. *Earth Planet. Sci. Lett.* **1980**, *49*, 149–165. [[CrossRef](#)]
53. Jin, X. Petrogenesis of the Shibaogou Granitoid Pluton and Evaluation of Metallogenic Potential, Western Henan Province. Master's Thesis, China University of Geosciences, Beijing, China, 2016. (In Chinese with English Abstract)
54. Zartman, R.E.; Doe, B.R. Plumbotectonics—The model. *Tectonophysics* **1981**, *75*, 135–162. [[CrossRef](#)]
55. Fan, H.R.; Xie, Y.H.; Zhao, R.; Wang, Y.L. Stable Isotope Geochemistry of Rocks and Gold Deposits in the Xiongershan Area Western Henan Province. *Contrib. Geol. Miner. Resour. Res.* **1994**, *9*, 54–64. (In Chinese with English Abstract)
56. Luo, M.J.; Zhang, F.M.; Dong, Q.Y.; Xu, Y.R.; Li, S.M.; Li, K.H. *Molybdenum Deposits in China*; Henan Science Technology Press: Zhengzhou, China, 1991; pp. 1–445. (In Chinese)
57. Ni, Z.Y.; Li, N.; Zhang, H.; Xue, L.W. Pb-Sr-Nd isotope constraints on the source of ore-forming elements of the Dahu Au-Mo deposit, Henan province. *Acta Petrol. Sin.* **2009**, *25*, 2823–2932. (In Chinese with English Abstract)
58. Zhao, T.P. The Characteristics and Genesis of the High-K Volcanic Rocks Within the Proterozoic Xiong'er Group at the Southern Margin of the North China Block. Ph.D. Thesis, Chinese Academy of Sciences, Beijing, China, 2000. (In Chinese with English Abstract)
59. Duan, S.G.; Xue, C.J.; Liu, G.Y.; Yan, C.H.; Feng, Q.W.; Song, Y.W.; Gao, B.Y. Geology, fluid inclusions and stable isotopic geochemistry of Bailugou Pb-Zn deposit in Luanchuan area, Henan Province. *Miner. Depos.* **2010**, *29*, 810–826. (In Chinese with English Abstract)
60. Zhang, Z.Q.; Zhang, G.W.; Liu, D.Y.; Wang, Z.Q.; Tang, S.H.; Wang, J.H. *Isotopic Geochronology and Geochemistry of Ophiolites, Granites and Clastic Sedimentary Rocks in the Qinling Orogenic Belt*; Geological Publishing House: Beijing, China, 2006; pp. 1–348. (In Chinese)
61. Barbarin, B. A review of the relationships between granitoid types, their origins and their geodynamic environments. *Lithos* **1999**, *46*, 605–626. [[CrossRef](#)]
62. Batchelor, R.A.; Bowden, P. Petrogenetic interpretation of granitoid rock series using multicationic parameters. *Chem. Geol.* **1985**, *48*, 43–55. [[CrossRef](#)]
63. Pearce, J. Sources and settings of granitic rocks. *Episodes* **1996**, *19*, 120–125. [[CrossRef](#)]
64. Harris, N.B.W.; Pearce, J.A.; Tindle, A.G. Geochemical characteristics of collision-zone magmatism. In *Collision Tectonics*; Coward, M.P., Ries, A.C., Eds.; Geological Society Special Publication: London, UK, 1986; Volume 19, pp. 67–81.
65. Chen, Y.J.; Li, C.; Zhang, J.; Li, Z.; Wang, H.H. Sr and O isotopic characteristics of porphyries in the Qinling molybdenum deposit belt and their implication to genetic mechanism and type. *Sci. China Ser. D* **2000**, *43*, 82–94. [[CrossRef](#)]
66. Chappell, B.W.; White, A.J.R.; Allen, C.M. Two contrasting granite types: 25 years later. *Aust. J. Earth Sci.* **2001**, *48*, 489–499. [[CrossRef](#)]
67. Hou, Z.Q.; Gao, Y.F.; Qu, X.M.; Rui, Z.Y.; Mo, X.X. Origin of adakitic intrusives generated during mid-Miocene east–west extension in southern Tibet. *Earth Planet. Sci. Lett.* **2004**, *220*, 139–155. [[CrossRef](#)]
68. Hu, F.Y.; Ducea, M.N.; Liu, S.W.; Chapman, J.B. Quantifying Crustal Thickness in Continental Collisional Belts: Global Perspective and a Geologic Application. *Sci. Rep.* **2017**, *7*, 7058. [[CrossRef](#)]
69. Dong, Y.P.; Yang, Z.; Liu, X.M.; Sun, S.S.; Li, W.; Cheng, B.; Zhang, F.F.; Zhang, X.N.; He, D.F.; Zhang, G.W. Mesozoic intracontinental orogeny in the Qinling Mountains, central China. *Gondwana Res.* **2016**, *30*, 144–158. [[CrossRef](#)]
70. Allegre, C.J.; Minster, J.F. Quantitative models of trace element behavior in magmatic processes. *Earth Planet. Sci. Lett.* **1978**, *38*, 1–25. [[CrossRef](#)]
71. Rollinson, H.R. *Using Geochemical Data: Evaluation, Presentation, Interpretation*; Routledge: London, UK, 2014; pp. 1–352.
72. Sisson, T.W. Hornblende-melt trace-element partitioning measured by ion microprobe. *Chem. Geol.* **1994**, *117*, 331–344. [[CrossRef](#)]
73. Peacock, S.M.; Rushmer, T.; Thompson, A.B. Partial melting of subducting oceanic crust. *Earth Planet. Sci. Lett.* **1994**, *121*, 227–244. [[CrossRef](#)]

74. Morata, D.; Oliva, C.; Cruz, R.D.L.; Suárez, M. The Bandurrias gabbro: Late Oligocene alkaline magmatism in the Patagonian Cordillera. *J. S. Am. Earth Sci.* **2005**, *18*, 147–162. [[CrossRef](#)]
75. Watson, E.B.; Green, T.H. Apatite/liquid partition coefficients for the rare earth elements and strontium. *Earth Planet. Sci. Lett.* **1981**, *56*, 405–421. [[CrossRef](#)]
76. Prowatke, S.; Klemme, S. Effect of melt composition on the partitioning of trace elements between titanite and silicate melt. *Geochim. Cosmochim. Acta* **2005**, *69*, 695–709. [[CrossRef](#)]
77. Martin, H.; Smithies, R.H.; Rapp, R.; Moyen, J.F.; Champion, D. An overview of adakite, tonalite-trondhjemite-granodiorite (TTG), and sanukitoid: Relationships and some implications for crustal evolution. *Lithos* **2005**, *79*, 1–24. [[CrossRef](#)]
78. Defant, M.J.; Drummond, M.S. Derivation of some modern arc magmas by melting of young subducted lithosphere. *Nature* **1990**, *347*, 662–665. [[CrossRef](#)]
79. Xiong, X.L.; Adam, J.; Green, T.H. Rutile stability and rutile/melt HFSE partitioning during partial melting of hydrous basalt: Implications for TTG genesis. *Chem. Geol.* **2005**, *218*, 339–359. [[CrossRef](#)]
80. Sen, C.; Dunn, T. Dehydration melting of a basaltic composition amphibolite at 1.5 and 2.0 GPa: Implications for the origin of adakites. *Contrib. Mineral. Petrol.* **1994**, *117*, 394–409. [[CrossRef](#)]
81. Rapp, R.P.; Watson, E.B.; Miller, C.F.; Haapala, I.; Condie, K.C. Partial melting of amphibolite/eclogite and the origin of Archean trondhjemites and tonalites. *Precambrian Res.* **1991**, *51*, 1–25. [[CrossRef](#)]
82. Depaolo, D.J.; Wasserburg, G.J. Petrogenetic mixing models and Nd-Sr isotopic patterns. *Geochim. Cosmochim. Acta* **1979**, *43*, 615–628. [[CrossRef](#)]
83. Wu, Y.B.; Zhou, G.Y.; Gao, S.; Liu, X.C.; Qin, Z.W.; Wang, H.; Yang, J.Z.; Yang, S.H. Petrogenesis of Neoproterozoic TTG rocks in the Yangtze Craton and its implication for the formation of Archean TTGs. *Precambrian Res.* **2014**, *254*, 73–86. [[CrossRef](#)]
84. Gao, S.; Yang, J.; Zhou, L.; Li, M.; Hu, Z.C.; Guo, J.L.; Yuan, H.L.; Gong, H.J.; Xiao, G.Q.; Wei, J.Q. Age and growth of the Archean Kongling terrain, South China, with emphasis on 3.3 Ga granitoid gneisses. *Am. J. Sci.* **2011**, *311*, 153–182. [[CrossRef](#)]
85. Zhang, G.W.; Meng, Q.R.; Lai, S.C. Tectonics and structure of Qinling orogenic belt. *Sci. China Ser. B* **1995**, *38*, 1379–1394.
86. Huang, X.L.; Wilde, S.A.; Yang, Q.J.; Zhong, J.W. Geochronology and petrogenesis of gray gneisses from the Taihua Complex at Xiong'er in the southern segment of the Trans-North China Orogen: Implications for tectonic transformation in the Early Paleoproterozoic. *Lithos* **2012**, *134–135*, 236–252. [[CrossRef](#)]
87. Luan, S.W.; Cao, D.C.; Fang, Y.K.; Wang, J.Y. Geochemistry of Xiaoqinling Gold Deposits. *Miner. Rocks* **1985**, *5*, 1–118. (In Chinese with English Abstract)
88. He, Y.H.; Zhao, G.C.; Sun, M.; Han, Y.G. Petrogenesis and tectonic setting of volcanic rocks in the Xiaoshan and Waifangshan areas along the southern margin of the North China Craton: Constraints from bulk-rock geochemistry and Sr-Nd isotopic composition. *Lithos* **2010**, *114*, 186–199. [[CrossRef](#)]
89. Wang, X.L.; Jiang, S.Y.; Dai, B.Z. Melting of enriched Archean subcontinental lithospheric mantle: Evidence from the ca. 1760 Ma volcanic rocks of the Xiong'er Group, southern margin of the North China Craton. *Precambrian Res.* **2010**, *182*, 204–216. [[CrossRef](#)]
90. Zhang, Z.Q.; Liu, D.Y.; Fu, G.M. *Study of Isotope Geochronology of Metamorphic Stratigraphy of North Qinling*; Geological Publishing House: Beijing, China, 1994; pp. 1–191. (In Chinese)
91. Chen, K.; Gao, S.; Wu, Y.B.; Guo, J.L.; Hu, Z.C.; Liu, Y.S.; Zong, K.Q.; Liang, Z.W.; Geng, X.L. 2.6–2.7 Ga crustal growth in Yangtze craton, South China. *Precambrian Res.* **2013**, *224*, 472–490. [[CrossRef](#)]
92. Zhu, X.Y.; Chen, F.K.; Li, S.Q.; Yang, Y.Z.; Nie, H.; Siebel, W.; Zhai, M.G. Crustal evolution of the North Qinling terrain of the Qinling Orogen, China: Evidence from detrital zircon U-Pb ages and Hf isotopic composition. *Gondwana Res.* **2011**, *20*, 194–204. [[CrossRef](#)]
93. Shi, Y.; Yu, J.; Santosh, M. Tectonic evolution of the Qinling orogenic belt, Central China: New evidence from geochemical, zircon U-Pb geochronology and Hf isotopes. *Precambrian Res.* **2013**, *231*, 19–60. [[CrossRef](#)]
94. Liu, X.Y.; Cai, J.H.; Yan, G.H. Litho geochemistry and Geochronology of Xiong'er Group Yanyaozhai Subvolcanics in the Southern Margin of the North China Craton and Their Geological Significance. *Acta Geol. Sin.* **2011**, *85*, 1134–1145. (In Chinese with English Abstract)
95. Yu, X.Q.; Liu, J.L.; Li, C.L.; Chen, S.Q.; Dai, Y.P. Zircon U-Pb dating and Hf isotope analysis on the Taihua Complex: Constraints on the formation and evolution of the Trans-North China Orogen. *Precambrian Res.* **2013**, *230*, 31–44. [[CrossRef](#)]
96. Xu, X.S.; Griffin, W.L.; Ma, X.; Reilly, S.Y.O.; He, Z.Y.; Zhang, C.L. The Taihua group on the southern margin of the North China craton: Further insights from U-Pb ages and Hf isotope compositions of zircons. *Mineral. Petrol.* **2009**, *97*, 43–59. [[CrossRef](#)]
97. Shi, Y.; Yu, J.H.; Xu, X.S.; Tang, H.F.; Qiu, J.S.; Chen, L.H. U-Pb ages and Hf isotope compositions of zircons of Taihua Group in Xiaoqinling area, Shaanxi Province. *Acta Petrol. Sin.* **2011**, *27*, 3095–3108. (In Chinese with English Abstract)
98. Niu, Y.L.; Zhao, Z.D.; Zhu, D.C.; Mo, X.X. Continental collision zones are primary sites for net continental crust growth—A testable hypothesis. *Earth-Sci. Rev.* **2013**, *127*, 96–110. [[CrossRef](#)]
99. Green, T.H.; McDonough, W.F.; Arndt, N.T.; Shirey, S. Significance of Nb/Ta as an indicator of geochemical processes in the crust-mantle system. *Chem. Geol.* **1995**, *120*, 347–359. [[CrossRef](#)]
100. Mao, S.D.; Chen, Y.J.; Zhou, Z.J.; Lu, Y.H.; Guo, J.H.; Qin, Y.; Yu, J.Y. Zircon geochronology and Hf isotope geochemistry of the granitoids in the Yangshan gold field, western Qinling, China: Implications for petrogenesis, ore genesis and tectonic setting. *Geol. J.* **2014**, *49*, 359–382. [[CrossRef](#)]

101. Zhou, Z.J.; Lin, Z.W.; Qin, Y. Geology, geochemistry and genesis of the Huachanggou gold deposit, western Qinling Orogen, central China. *Geol. J.* **2014**, *49*, 424–441. [[CrossRef](#)]
102. Zhou, Z.J.; Chen, Y.J.; Jiang, S.Y.; Zhao, H.X.; Qin, Y.; Hu, C.J. Geology, geochemistry and ore genesis of the Wenyu gold deposit, Xiaqingling gold field, Qinling Orogen, southern margin of North China Craton. *Ore Geol. Rev.* **2014**, *59*, 1–20. [[CrossRef](#)]
103. Chen, Y.J. The development of continental collision metallogeny and its application. *Acta Petrol. Sin.* **2013**, *29*, 1–17. (In Chinese with English Abstract)
104. Xu, Y.C.; Wang, G.W.; Gao, M.; Yang, W.D.; Yang, S.R.; Yun, H.; Wu, P.J.; Guo, N.N.; Feng, Y.T. Genesis of the Shibaogou Mo-Pb-Zn deposit in the Luanchuan ore district, China: Constraints from geochronology, fluid inclusion, and H-O-S-Pb isotopes. *Front. Earth Sci.* **2023**, *10*, 1032183. [[CrossRef](#)]
105. Irber, W. The lanthanide tetrad effect and its correlation with K/Rb, Eu/Eu\*, Sr/Eu, Y/Ho, and Zr/Hf of evolving peraluminous granite suites. *Geochim. Cosmochim. Acta* **1999**, *63*, 489–508. [[CrossRef](#)]
106. Mercer, C.N.; Reed, M.H.; Mercer, C.M. Time scales of porphyry Cu deposit formation; insights from titanium diffusion in quartz. *Econ. Geol.* **2015**, *110*, 587–602. [[CrossRef](#)]
107. Barra, F.; Alcota, H.; Rivera, S.; Valencia, V.; Munizaga, F.; Maksaev, V. Timing and formation of porphyry Cu-Mo mineralization in the Chuquicamata district, northern Chile; new constraints from the Toki cluster. *Miner. Depos.* **2013**, *48*, 629–651. [[CrossRef](#)]
108. Ossandón, C.G.; Fréaut, C.R.; Gustafson, L.B.; Lindsay, D.D.; Zentilli, M. Geology of the Chuquicamata mine: A progress report. *Econ. Geol.* **2001**, *96*, 249–270. [[CrossRef](#)]
109. Williams-Jones, A.E.; Migdisov, A.A. Experimental Constraints on the Transport and Deposition of Metals in Ore-Forming Hydrothermal Systems. *Econ. Geol.* **2014**, *18*, 77–95.

**Disclaimer/Publisher’s Note:** The statements, opinions and data contained in all publications are solely those of the individual author(s) and contributor(s) and not of MDPI and/or the editor(s). MDPI and/or the editor(s) disclaim responsibility for any injury to people or property resulting from any ideas, methods, instructions or products referred to in the content.